Perovskite Oxide Catalysts for Advanced Oxidation Reactions

Kai Wang, Chen Han, Zongping Shao,* Jieshan Qiu, Shaobin Wang, and Shaomin Liu*

Meeting the escalating demand for clean water resources is one of the key challenges to ensure a sustainable future. Catalysis plays an important role to advance the chemical reactions required for wastewater efficient remediation. How to exploit high-performance catalysts to boost the pivotal reaction kinetics always attracts researchers' enthusiasm. Perovskite oxides as a novel class of functional materials can be tuned to confer compositional flexibilities and provide rich and unique structural properties. As the rising-star material, it has been widely probed for electrocatalysis, photocatalysis, and membrane-catalysis for energy conversion, but received less attention in water treatment. In this review, the advances of perovskite oxides for advanced oxidation processes (AOPs) in water remediation are comprehensively elaborated. A fundamental understanding of the crystal structures and properties of perovskite oxides as well as the basic principles of AOPs is firstly provided. Then, emphasis is placed on how to tune the perovskite oxides to suit various AOPs. The strategies to design novel perovskite oxides to enhance the catalytic activities in AOPs have been highlighted. It is expected that after reading this review, readers will have a clearer vision of the background, the state of the art development, and general guidelines for future directions regarding research in this area.

1. Introduction

Our contemporary society is experiencing unprecedented severe challenges from energy crisis and environmental deterioration due to the over-industrialization and thus a new infrastructure of sustainability is required to continue the civilization. To tackle the dilemma of economic development and environmental conservation, a joint effort should be made from

the exploitation of clean energy resources and deployment of advanced remediation schemes. As the typical and promising environmental cleaning technologies, advanced oxidation processes (AOPs) by activating peroxides to generate reactive oxygen species (ROS) have been widely studied to oxidize the various toxic organic components in water body. Great efforts have been devoted to exploring the green and more efficient catalysts for AOPs. These catalysts include various metals, metal oxides, metal nitrides, and carbonaceous (metal-free) materials.[1] The former metal-containing catalysts are featured by their high activity but may be suffered from the high material cost in case of precious metals or the possible second pollution due to the leaching of toxic metals. On the contrary, the latter metal-free catalysts are generally characterized by their low reaction efficiency. One compromising strategy for catalyst design is to choose these naturally abundant metallic elements but in stable crystal structure (i.e., oxidation states) to reduce their leaching or toxicity. Among the complex oxide structures to accommodate multiple metal elements, spinel and perovskite oxides are most widely studied due to their interesting properties like ferromagnetism, ferroelectricity, piezoelectricity, high temperature superconductivity, electronic/ionic conductivity, and so on.[2–4] Most of these properties are stemmed from their electrons in d/f orbitals of metals, oxygen defects, or various crystal structure distortions. In particular, perovskite oxides as the emerging star functional material can also be applied as catalysts due to their high design flexibility, controllable defects to create ionic or electronic conductivities, tunable surface property, and stability.[5] These perovskite oxide catalysts can be used for environmental catalysis for clean combustion to remove NO, CO, SO or uncombusted hydrocarbons, alkane partial oxidations, electrocatalysis for oxygen reduction or evolution reaction (ORR and OER) for energy conversion and storage, photocatalysis in water splitting for hydrogen production and membrane catalysis for chemical separation and production.[6,7] Good review articles in these areas are already available for a comprehensive understanding of the different roles playing by the perovskite oxides in these different reaction systems.[8–11]

In this review, we attempt to provide a comprehensive account of using perovskite oxides as the activation catalysts for AOPs for environmental remediation from the available

K. Wang, C. Han, Prof. Z. P. Shao, Prof. S. M. Liu
WA School of Mines: Minerals, Energy and Chemical Engineering
Curtin University
Perth, Western Australia 6102, Australia
E-mail: zongping.shao@curtin.edu.au; shaomin.liu@curtin.edu.au
Prof. J. S. Qiu, Prof. S. M. Liu
Beijing Advanced Innovation Centre for Soft Matter Science
and Engineering
College of Chemical Engineering
Beijing University of Chemical Technology
Beijing 100029, China
Prof. S. B. Wang
School of Chemical Engineering and Advanced Materials
The University of Adelaide
Adelaide, South Australia 5005, Australia

ADVANCED
SCIENCE NEWS
www.advancedsciencenews.com

ADVANCED
FUNCTIONAL
MATERIALS
www.afm-journal.de

literature up to 2020. The fundamentals, principles, research advances, mechanisms, advantages or disadvantages, and crucial problems for all kinds of perovskite oxides used in AOPs are discussed. It is expected this review will provide necessary background and general guidelines to those who are involved or about to be involved in this research field.

2. Fundamentals of Perovskite Oxides and AOPs

2.1. Perovskite Oxide Materials

2.1.1. Crystal Structure

Single Perovskite Oxide: Perovskite materials are defined as the class of compounds that share similar crystal structure including halide perovskite, organic perovskite, and perovskite oxides, where the former two are popular materials being applied in solar cells. Herein, the review is mainly focusing on perovskite oxide materials. Perovskite oxides originally are referred to the calcium titanium oxides mineral with a composition of $CaTiO_3$. Later, the name of perovskite oxides has been extended to include a series of multiple metal oxides (ABO_3) with similar cation arrangement as $CaTiO_3$. In a typical ABO_3 structure, the ionic size of A is larger than B cations. One advantage of perovskite oxides is the flexibility to adopt various kinds of metal elements either at A- or B-site. A-site cations can be chosen from the alkaline, alkaline-earth, or lanthanide rare-earth metal elements while B-site is often occupied by the transition metals (TMs). To date, it has been reported that more than 90% of metallic elements from periodic table have been successfully incorporated into the lattice of ABO_3 perovskite.[9]

The ideal perovskite oxide is a symmetric cubic structure as shown in **Figure 1**a, where the B site is coordinated with six oxygens and presented as the corner-sharing BO_6 octahedrons

and the larger A-site cations are accommodated in the interstices among eight BO_6 octahedrons. The stability and physical properties of ABO_3 perovskite are more determined by the B-site metal ions (i.e., the ionic size, valence, and spin states). In order to maintain the stability of the octahedron coordination, the B-site TM cations should be generally larger than 0.51 Å. Moreover, the size of A-site cations affects the symmetry of ABO_3 structure and such a deviation may cause octahedron distortion from the pristine ideal cubic structure. Therefore, a tolerance factor (*t*) based on empirical equation was introduced by Goldschmidt to measure the structure deviation from the geometry of cubic unite cell, which is defined by Equation (1).[12]

$$t = \frac{(R_A + R_O)}{\sqrt{2} \cdot (R_B + R_O)} (0.75 < t < 1.13) \tag{1}$$

Where R_A, R_B, and R_O stand for the radius of A-, B-, and O-site ions, respectively. The cubic structure can be stabilized when *t* is in the range of 0.75 to 1.13. The octahedral factor (R_B/R_O) is also applied to evaluate the phase stability due to the significant role of BO_6 octahedron in the ABO_3 skeleton.[13] In addition to the geometrical considerations, the structural stability is associated with many other factors like coulombic interaction, basicity, or acidity of the metal oxides which translates to possible chemical reactions with the surrounding atmosphere.[14,15]

Perovskite Oxides Derivatives: Compositional flexibility gives rise to the formation of a series of derivatives of normal perovskite oxides (ABO_3) with ordered and lamellar structures, such as double, quadruple, Rullesden–Popper (R–P), Dion–Jacobson (D–J), and Aurivillius perovskite oxides.[7,16,17] For example, partial substituting cations with A′ or B′ leads to the formation of $A_{1-x}A'_xBO_3$ or $AB_xB'_{1-x}O_3$. Only if $x \approx 0.5$ and cation dopant (A′ or B′) shows significant difference in atomic size and/or valence state to the host atoms (A or B), they would arrange in order and thus result in the double perovskite with a nominal composition of $AA'B_2O_6$ or $A_2BB'O_6$ (Figure 1b).[18] Another type of A-site
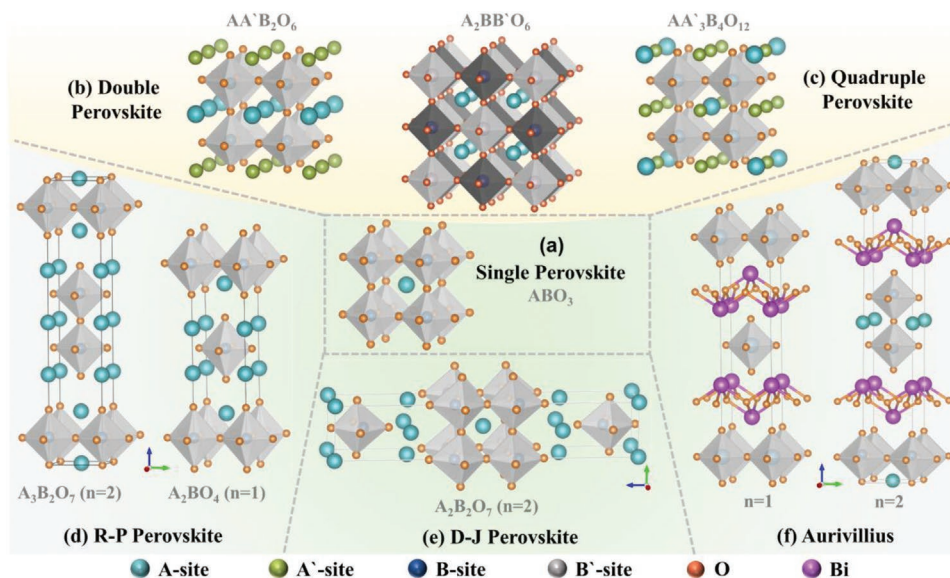
Figure 1. A schematic depicting of the crystal structures of a) single (space group: *Pm-3m*), b) double (space group: *P4/mmm* for $AA'B_2O_6$ and *Fm-3m* for $A_2BB'O_6$), c) quadruple (space group: *Im-3m*), d) R–P, e) D–J, and f) Aurivillius (space group: *I4/mmm*) perovskite oxides.

cation-ordered perovskite oxides, that is, quadruple perovskite oxides, describe the compounds constructed by the framework of BO_6 octahedra and $A'O_4$ squares as well as the interstitial A-site cations (Figure 1c), giving a nominal composition of $AA'_3B_4O_{12}$.[19] Different from the single and double perovskites that A-site can only accommodate alkaline, alkaline-earth, or lanthanide rare-earth metal elements, the A′-site in quadruple perovskite can be occupied by TMs, such as Cu and Mn.[19]

Lamellar perovskite oxides derived from the basic ABO_3 structure include R–P, D–J, and Aurivillius peroxide oxides with the formula of $A'_2[A_{n-1}B_nO_{3n+1}]$, $A'[A_{n-1}B_nO_{3n+1}]$, and $(Bi_2O_2)(A_{n-1}B_nO_{3n+1})$, respectively.[20,21] Typically, these layered perovskite oxides consist of alternating n-layer ABO_3 perovskite slabs and rock salt layers, and all layers are stacked along the c-axis (Figure 1d–f).[22] Therefore, layered perovskite oxides have even more rich properties that are stemmed not only from the constituent elements, but also from the physical structure such as the unique structural arrangement and number of perovskite layers.

2.1.2. Properties of Perovskite Oxides

Inspired by the abundant properties and their controllable characters of perovskite oxides, research interests mainly focused on tailoring properties to improve the catalytic performance, such as compositional design and defects engineering. Herein, we summarize the main characters of perovskite oxides that benefit catalytic process.

Redox Property: Perovskite oxides containing TMs such as Fe, Co, Ni, Mn, and Cu are featured with multiple oxidation states of these B-site TMs, which are active for both catalytic reduction and oxidation reactions, like NO_x decomposition, organics oxidation, and electrochemical redox reaction.[5,23] Typically, in AOPs, a straightforward correlation between catalytic activity and the proportion of low-valence-TMs (Fe^{2+}, Co^{2+}, Cu^{1+}, Ni^{2+}, Mn^{3+}, etc.) is established, indicating the real active centers are surface-reduced TMs (B^{n+}).[24] Because peroxides activation over perovskite oxides is triggered by withdrawing electrons from

catalysts, these electron-rich TMs serve as donor to drive the peroxides decomposition and ROS generation. On the other hand, the oxidized TMs ($B^{(n+1)+}$) during the catalytic process require fast reduction so as to maintain the catalytic activity, which indirectly determines the catalytic efficiency and stability of perovskite oxides. In case of oxidation reactions, the active sites of oxidized TMs experience the redox process as well. Hence, redox activity of perovskite oxide is of vital importance either in catalytic reduction or oxidation reactions as it basically determines the catalytic performance.

In perovskite oxides, due to the strong overlapping between B-site ions and O^{2-} orbital resulted from the unique structure arrangement, the electronic conductivity is realized by B-site cation lattice (B−O−B bonds), known as the Zerner double exchange regime:[25]

$$B^{n+} - O^{2-} - B^{(n+1)+} \rightarrow B^{(n+1)+} - O^{-} - B^{(n+1)+} \rightarrow B^{(n+1)+} - O^{2-} - B^{n+} \tag{2}$$
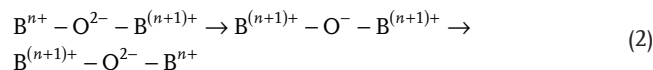
According to this process, the electronic conduction relies on the B−O−B network and valence alternation of TMs, which thus greatly promote the operation of $B^{(n+1)+}/B^{n+}$ redox cycle. Another important factor that contributes to the redox property is the outstanding ions conductivity in perovskite oxides, where oxygen intercalation, emission, and lattice O^{2-} migration could give rise to good bulk redox activity.[26] Briefly, the features of multiple valences of TMs and the unique structure arrangement, as well as good ion conductivity of perovskite oxides, jointly enhanced the $B^{(n+1)+}/B^{n+}$ redox cycle.

In light of these properties, perovskite oxides have been broadly applied in catalytic redox reactions. For example, Su et al. compared the catalytic activity between double perovskite oxide $PrBaCo_2O_{5+\delta}$ (PBC) and commercial Co_3O_4 by employing them as hetero-activators for peroxymonosulfate (PMS) salt activation in AOPs.[27] It was surprisingly found that PBC exhibited ≈196 times higher turnover frequency (TOF) to the commercial Co_3O_4, which can be greatly attributed to the outstanding redox activity of perovskite. The O_2-TPD profiles (**Figure 2a**) show that the thermal reduction of Co^{3+} starts from 300 °C
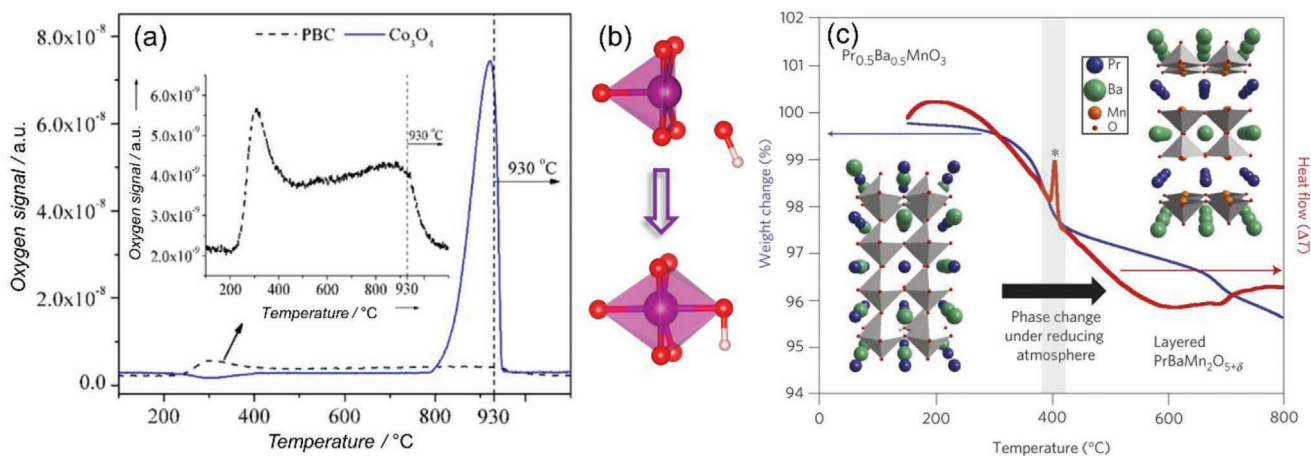
Figure 2. a) The O_2-TPD profiles of $PrBaCo_2O_{5+\delta}$ (PBC) and Co_3O_4. Reproduced with permission.[27] Copyright 2017, American Chemical Society. b) The schematic illustration of OH^- adsorption on deficient MnO_5. Reproduced with permission.[38] Copyright 2014, American Chemical Society. c) Phase transition of $Pr_{0.5}Ba_{0.5}MnO_3$ to deficient $PrBaMn_2O_5$ at reducing atmosphere. Reproduced with permission.[16] Copyright 2014, Nature Publishing Group.

for PBC while the reduction peak appears at 800 °C for Co_3O_4, signifying a much easier transition of Co^{3+}/Co^{2+} redox cycle of perovskite. Demont et al. used Mn-based perovskite oxides for CO_2 catalytic reduction and observed that CO production ability relies on the Mn^{3+}/Mn^{4+} redox cycling ability.[28] Moreover, the authors found that partial substitution either at A- or B-site would lead to positive effects on the reduction of high-valence Mn and thus result in better catalytic performance. An identical phenomenon was also reported by Irusta et al. who explored the intrinsic mechanism of the improved redox property of Sr-doped $LaMnO_3$ and $LaCoO_3$ for catalytic removal of volatile organic pollutants.[29] Partial introduction of Sr at A-site could reduce the crystallinity of $LaMnO_3$ and $LaCoO_3$, resulting in a more feasible reduction process. Another factor, that is, sintering temperature in perovskite oxides synthesis process, governs the crystallinity which may cause influence on the redox properties. The mechanism of various external factors and A-site dopants to promote redox process has been well summarized by Royer et al.[9] As commented by them, the surface oxygen binding energy, oxygen mobility, crystallinity, and ion size of A-site are the key parameters determining the reducibility of B-site TMs. Recently, Sun et al. introduced the A-site cation defects to $La_{0.6}Sr_{0.3}Cr_{0.85}Ni_{0.15}O_{3-\delta}$ and investigated their effects on redox ability.[30] In the presence of cation deficiency, the reduction temperature of Ni^{3+} to Ni^{2+} and Ni^{2+} to Ni^0 is significantly lowered compared to the full stoichiometry component, indicating the promoted Ni^{3+}/Ni^{2+} redox cycle by A-site cation defects. Generally, the oxygen vacancy would be spontaneously generated with the creation of cation defects to maintain charge neutrality. Such defects feature is beneficial for the lattice oxygen migration, emission, and intercalation, consequently giving rise to an enhanced redox ability of B-site TMs. Along with A-site modulation, B-site dopants are able to assist the redox cycle directly by the means of forming conjunctive redox pairs with the host TMs. For example, the Co-based perovskite oxides with Fe or Cu dopants manifested excellent catalytic behavior due to the improved redox ability.[31,32] The standard reduction potential of Fe^{3+}/Fe^{2+} and Co^{3+}/Co^{2+} are 0.77 and 1.81 V, respectively. Thus the reduction of Co^{3+} to Co^{2+} by Fe^{2+} with reduction energy of 1.04 V is favored thermodynamically.

In addition to the conventional TM-cations redox couples, lattice oxygen near the perovskite surface and adsorbed molecule oxygen were proposed as an important redox pair for electrochemical reaction based on the operando X-ray absorption spectroscopy investigation.[33] It was observed that $e_g\uparrow$ (a narrow electronic state of O 2p character close to the Fermi level) exchanges electrons with oxygen adsorbates. More specifically, strong hybridization of TM 3d and O 2p orbitals resulting in e_g and t_{2g} molecule orbitals, corresponding to the σ and π TM—O bonds, respectively. The depopulation of the electrons in $e_g\uparrow$ orbital near Femi level and annihilation of oxygen vacancies occurred with the anodic polarization (oxygen evolution process). And with the increment of applied overpotential, electrons in $e_g\uparrow$ orbital were gradually depleted, suggesting the oxidation of perovskite. On the other hand, for the cathode polarization (oxygen incorporation), the population of the electrons in $e_g\uparrow$ corresponds to the reduction of perovskite. The relationship between $e_g\uparrow$ orbital electronic states

and overpotential powerfully proved the oxygen redox-active center because the unoccupied $e_g\uparrow$ orbital is a character of O 2p arising from covalency. Recently, another study that combined the operando experiments and kinetics modeling also demonstrates that the active oxygen redox gives rise to the high catalytic activity in oxygen electrocatalysis.[34]

Oxygen Non-Stoichiometry: In perovskite oxides, the partial substitution either at A or B-site by foreign cations with varied valences and size would lead to the occurrence of oxygen non-stoichiometry ($A_{1-x}A'_xB_{1-y}B'_yO_{3\pm\delta}$): oxygen access ($+\delta$) or vacancy ($-\delta$). According to the charge neutrality principle, the total cation valence is not equal to +6 in the case of oxygen nonstoichiometry. δ is related to many factors, that is, the cation content, the cation valence and spin state, cation size, and the surrounding environment (temperature and gas atmosphere). For oxygen vacancy, δ value is usually less than 0.5; in other words, the empty sites (vacancies) in the oxygen position in the perovskite lattice is usually less than 17%, more than which would collapse the perovskite structure.[35] Oxygen vacancy with localized electrons and the nature of unsaturated coordination is the ideal reactive site for intermediates and peroxide molecules binding and ionic/electronic conductivity, which is the most common and desirable characteristic of perovskite oxides. It is associated not only with catalytic reaction applications but also with the oxygen/proton transport systems, like oxygen permeation membranes and membrane reactors.[36] Oxygen vacancy formation would result in the redistribution of the electrons. The electron-deficient nature of oxygen vacancies enables them as Lewis acid site acting as electron acceptor, while the oxygen vacancy-induced electron localization of B-site TMs nearby occurs, both of which have profound impacts on catalysis.[37] Up to now, many papers have revealed the vital roles of oxygen vacancy in electrochemical system and AOPs.[38,39] For instance, a direct correlation was established between OER-specific activity and the content of surface oxygen vacancies on $La_{1-x}Sr_xFeO_{3-\delta}$ by She and his co-workers, indicating the determining role of surface oxygen vacancy on OER activity.[40] Meanwhile, Wang et al. also observed the resemblance between the trend of OER performance and surface oxygen vacancy-related highly oxidative oxygen species (O^-/O_2^{2-}) on Co-based perovskites.[41] The mechanism behind such enhancement of OER activity under alkaline media was explored by Kim, who synthesized the ordered oxygen-deficient $Ca_2Mn_2O_5$ perovskite for oxygen catalytic evolution.[38] In comparison with the fully coordinated MnO_6 octahedron in perovskite, the deficient MnO_5 structure with an oxygen vacancy could promote the adsorption of OH^- (Figure 2b). Thus oxygen vacancy in MnO_5 subunit being as the active site facilitates the bonding of OH^- on Mn^{3+}, which initiates the OER process. Other pioneering works have also proved the indispensable character of oxygen defects in AOPs. And many attempts have been devoted to disclosing the working principles of oxygen defects in peroxide (PMS, O_3, O_2, and H_2O_2) activation.[42,43] A more detailed summarization of the oxygen vacancy-promoted peroxide activation will be given in Section 3.

Surface oxygen vacancy is the active site for both organics adsorption and peroxides activation, a very important step for various catalytic systems. Therefore, defect engineering is

pursued extensively. Aliovalent doping is the most frequently used technique for oxygen vacancy creation. For example, Sr, Ca, and Ba are popular A-site dopants for the type of $Ln^{3+}M^{3+}O_3$ (Ln = La, Pr, Eu) perovskite oxides with derivatives such as $La_{1-x}Sr_xMO_{3-\delta}$ (M = Co or Ni),[44,45] $La_{1-x}Ba_xInO_{3-\delta}$,[46] and $La_{1-x}Ca_xCrO_{3-\delta}$.[47] B-site dopants such as Cu, Mg, Zn, and Sc have also been proved to promote oxygen defect generation.[48–50] Besides the doping approach, A or B-site cation nonstoichiometry control is also demonstrated as an efficient way to tailor the oxygen vacancy content. For instances, a series of cation-deficient $La_{1-x}FeO_{3-\delta}$ (x = 0.02, 0.05, 0.1, and 0.2),[51] $Sr_{0.95}Nb_{0.1}Co_{0.9}O_{3-\delta}$,[52] $La_{0.4}Sr_{0.55}Co_{0.2}Fe_{0.6}Nb_{0.2}O_{3-\delta}$,[53] $(Ba_{0.5}Sr_{0.5})_{1-x}(Co_{0.8}Fe_{0.2})O_{3-\delta}$[25] and $La_{2-x}CoTiO_{6-\delta}$ (x < 0.2)[54] with improved surface oxygen vacancy concentration were harvested by altering the molar ratio of A/B from 1. All of these materials exhibit promising properties in their applications due to the oxygen defects induced by cation deficiency. Of course, the large deviation of A/B ratio from unity would lead to the formation of impurities and phase segregation, the cation defect degree is often less than 10% molar ratio empirically.[55] The ionic radius also has influence on the oxygen non-stoichiometry. For example, when A-site cations are substituted by larger-sized metal ions, the B-site cations tend to increase the radius by lowering their oxidation states to stabilize the perovskite structure as reflected by the tolerance factor equation. The transferring of metal valence states from high to low oxidation states would increase the oxygen non-stoichiometry (or vacancy concentration).

Additionally, reducing atmosphere or elevated operation temperature can be adopted for oxygen vacancy creation by decreasing the valence of A or B-site TMs. For example, under the reducing atmosphere (containing 5% H_2) and mild temperature, $Pr_{0.5}Ba_{0.5}MnO_3$ could be transited to the oxygen vacancy-rich $PrBaMn_2O_5$ layered double perovskite (Figure 2c).[16] Similarly, the phase transition of $CaMnO_3$ to $Ca_2Mn_2O_5$ double perovskite could occur by the reduction of Mn^{4+} to Mn^{3+} in perovskite under reducing atmosphere or high temperatures accompanying the formation of a high amount of oxygen vacancies.[38] This is the working principle for oxygen storage or release using perovskite oxides for chemical looping in clean combustion.[56] Other advanced surface treatment methods, like UV radiation[57] and plasma etching[58] can be the alternative techniques employed in defects engineering.

Compared to oxygen vacancy, another kind of oxygen defects-oxygen excess has received less attention as its formation is not thermodynamically favorable.[59] Oxygen access is observed in some perovskite oxides by the incorporation of interstitial oxygen. For example, Mn-containing perovskite oxides of $LaMnO_{3+\delta}$,[60] Sr-doped $La_{1-x}Sr_xMnO_{3+\delta}$[59] and A-site deficient $La_{0.9}MnO_{3+\delta}$[61] display the possibility to accommodate access oxygen by a post-treatment method via sintering under high temperature and oxygen partial pressure.[62] The achieved δ value is up to 0.265. Such kind of oxygen storage feature and the high mobility of interstitial oxygen enables its applications in chemical looping or energy storage/conversion.[60]

Tunable Electronic Configuration: Considering hundreds of perovskite oxides with varied compositions can be used as catalysts for many applications. Researchers have paid tremendous efforts to screen the most valuable perovskite-based catalysts for OER, ORR, and AOPs by optimizing the compositions. Based on the abundant experimental data and theoretical exploration, electronic configuration is revealed to be one of the most important factors influencing catalytic performance. Shao-Horn's group introduced a molecular orbital theory to describe the perovskite activity.[63] They established the correlation between the e_g occupancy and OER activity, where the e_g filling number close to unity gives rise to outstanding OER activity. Thus a volcano-shaped correlation was proposed as illustratively shown in **Figure 3**a. The $Ba_{0.5}Sr_{0.5}Co_{0.8}Fe_{0.2}O_{3-\delta}$ (BSCF) at the peak position exhibited even an order of magnitude higher intrinsic activity to the benchmark IrO_2 owing to its e_g filling number of ≈1.2. This principle has also been extended to the ORR[64] (Figure 3b) and PMS-based AOPs[65] (Figure 3c). The e_g orbital electronic state is mainly determined by the B-site TMs' oxidation states and spin state, which are greatly impacted by the chemical composition. A- and/or B-site partial substitution would lead significant impact on the valence and spin states of TMs at B-site. For example, Zeng et al. noticed that the valence and spin state of Co in $SrCo_{0.95}M_{0.05}O_{3-\delta}$ are varied with different M dopants.[66] Therefore, this theory would guide the catalysts rational design in terms of the composition tailoring. Other physicochemical properties, like ferromagnetic property, adsorption, surface acidity, and mixed electron-ion conductivity of perovskite oxides render them have further applications.[67,68]
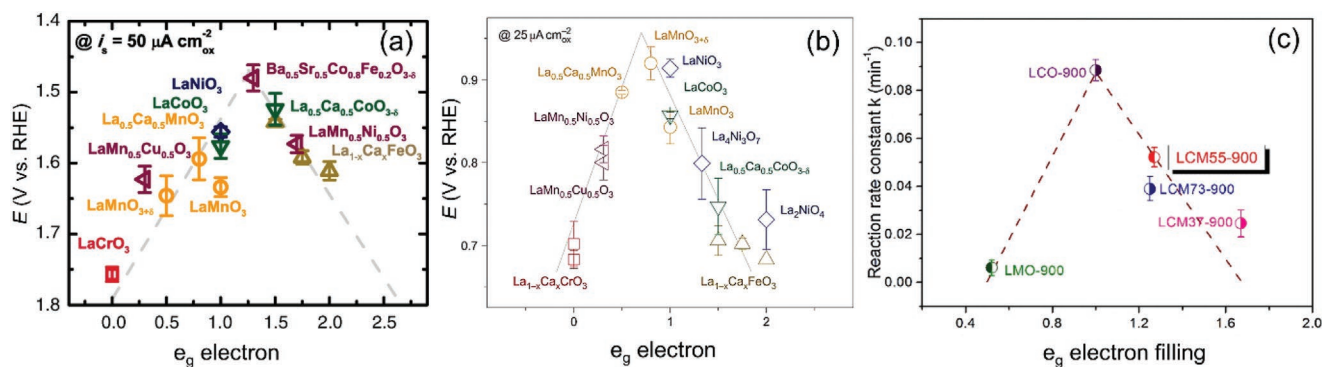
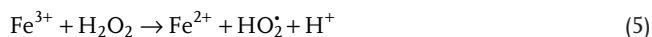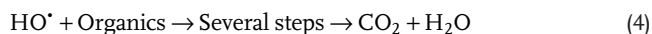**Figure 3.** The correlation of e_g filling number with: a) OER activity. Reproduced with permission.[63] Copyright 2011, AAAS. b) ORR activity. Reproduced with permission.[64] Copyright 2011, Nature Publishing Group. c) PMS activation efficiency. Reproduced with permission.[65] Copyright 2018, Elsevier.

2.2. Advanced Oxidation Processes (AOPs)

AOPs was first proposed in 1987 as an emerging water treatment technology relying on the in situ generation of powerfully oxidative ROS, like hydroxyl radicals ($^{\bullet}OH$), sulfate radicals ($SO_4^{\bullet-}$), and singlet oxygen ($^1O_2$) via peroxides activation.[69] Since then, AOPs have gained enormous development and own a broad of research branches. According to the types of employed peroxides and reaction system, AOPs can be divided into Fenton/Fenton-like system, persulfate-based reactions, catalytic ozonation process, catalytic wet air oxidation (CWAO) process, and so on. On the other hand, AOPs can also be classified based on a variety of external stimulation methods, such as photo-, peroxide-, electron-, ultrasound-, and plasma-based processes. Meanwhile, some hybrid systems by the combination of these peroxides or activation approaches have also been explored, such as photo-Fenton, electron-Fenton, UV/H_2O_2, and H_2O_2/O_3 systems. In short, the main purpose of these attempts is to boost ROS productivity and thus to improve the decomposition and mineralization efficiency of water-containing organic pollutants. In this part, some fundamentals of several popular AOPs are briefly introduced.

2.2.1. Fenton-Like System

In the classic Fenton system, divalent iron ions (Fe^{2+}) act as homogenous catalysts for activation of H_2O_2 (known as the Fenton reagent) to produce $^{\bullet}OH$ with a standard reduction potential of 2.8 V, which shows high destruction rates towards all organic molecules without selectivity. The generally recognized radical production and organic degradation pathways of conventional Fenton process are presented in the following Equations (3–8).[70] Initially, $^{\bullet}OH$ is generated from H_2O_2 decomposition mediated by electron transfer activities among Fe^{2+} and H_2O_2 (Equation (3)). Then the chemical attack of organics from active $^{\bullet}OH$ occurs (Equation (4)), while the catalysts are regenerated via Equation (5) (reaction with H_2O_2) and Equations (6–8) (reaction with organic intermediates RH).
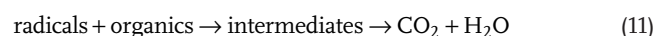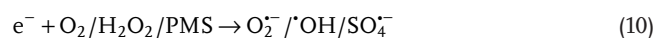
$$Fe^{2+} + H_2O_2 \rightarrow Fe^{3+} + HO^{\bullet} + HO^- \tag{3}$$

$$HO^{\bullet} + Organics \rightarrow Several\ steps \rightarrow CO_2 + H_2O \tag{4}$$

$$Fe^{3+} + H_2O_2 \rightarrow Fe^{2+} + HO_2^{\bullet} + H^+ \tag{5}$$

$$RH + HO^{\bullet} \rightarrow R^{\bullet} + H_2O \tag{6}$$

$$R^{\bullet} + Fe^{3+} \rightarrow R^+ + Fe^{2+} \tag{7}$$

$$R^+ + HO^- \rightarrow R - OH \tag{8}$$

Benefiting from the homogeneous catalysis, the high yield of $^{\bullet}OH$ radicals and their fast reaction rate with most organic and inorganic solutes give rise to a prominent AOPs efficiency. Nevertheless, the harsh working environment (i.e., narrow pH range and fewer background components) and the drawbacks of homogeneous catalysis lead to the sludge generation of Fenton system, which suppresses its further development and applications.[71] To eliminate these issues, research interests have been shifted to heterogeneous catalysis. As a result, heterogeneous Fenton-like system is considered a promising alternative with fewer energy inputs and reduced secondary contamination.[72] In Fenton-like system, metal-based and metal-free materials are dispersed in aqueous system to activate H_2O_2 and produce $^{\bullet}OH$ for AOPs.[73] The mechanism of H_2O_2 activation in hetero-Fenton is similar to the conventional Fenton system via the pathways of i) electron-donating from catalyst, ii) H_2O_2 decomposition and $^{\bullet}OH$ generation, iii) organics elimination and catalyst regeneration. Besides the dominant electron-transfer mediation, the other functions from hetero-catalyst would assist the H_2O_2 decomposition due to the defects features in metal oxides or carbon-based catalysts.[71]

2.2.2. Photocatalysis-Based AOPs

As an effective solar-energy utilization approach, photocatalysis attracts intensive research enthusiasm for clean energy conversion and environment purification since the path-breaking work by Fujishima and Honda in 1972.[74] Tremendous work has been dedicated to photocatalysis for H_2 and O_2 evolution, CO_2 reduction and other energy conversion-related areas, while photocatalysis-based AOPs constituents only a small part. In photocatalytic AOPs, photon (with higher or equal energy to bandgap energy) absorption by semiconductor would promote the excitation of electrons (e^-) from the valence band (VB) to the conduction band (CB), thus leaving holes (h^+) in VB (Equation (9)). Afterward, the excited e^- with high reduction ability would be captured by the dissolved oxygen to form superoxide radicals ($O_2^{\bullet-}$) which can attack organic molecules (Equations (10,11)). Or in some joint systems, like photo-Fenton or photo-PMS processes, the excited electrons may directly interact with H_2O_2 or PMS for free radicals generation. Simultaneously, holes in VB are powerful oxidizing agents that would instantly oxidize organic components or water to produce $^{\bullet}OH$ (Equation (12,13)). Also, some excited electrons and holes would recombine. Therefore, the excitation of photocatalyst and photo-degradation process can be expressed via the following equations.[75]

$$semiconductor + h\nu \rightarrow e^- + h^+ \tag{9}$$

$$e^- + O_2/H_2O_2/PMS \rightarrow O_2^{\bullet-}/^{\bullet}OH/SO_4^{\bullet-} \tag{10}$$

$$radicals + organics \rightarrow intermediates \rightarrow CO_2 + H_2O \tag{11}$$

$$h^+ + organics \rightarrow intermediates \tag{12}$$

$$h^+ + OH^- \rightarrow {}^{\bullet}OH \tag{13}$$

The success of harvesting solar energy lies in material science because the key point of solar energy conversion efficiency is determined by the properties of photocatalyst, especially the

**ADVANCED
SCIENCE NEWS**

www.advancedsciencenews.com

**ADVANCED
FUNCTIONAL
MATERIALS**

www.afm-journal.de

bandgap energy and charge carrier separation. As a result, technologies and material design have attracted enormous research interests in reducing the bandgap and the electron-hole recombination rate.

2.2.3. Sulfate Radical-Based AOPs

Owing to the higher standard oxidative potential ($SO_4^{\bullet-}$, 2.5–3.1 V versus $^{\bullet}OH$, 2.7 V) and longer half-life ($SO_4^{\bullet-}$, 30–40 ms versus $^{\bullet}OH$, <1 μs) of sulfate radicals, extensive works have been done to develop alternative sulfate radical-based AOPs ($SO_4^{\bullet-}$-AOPs) via activation of peroxydisulfate (PDS) and peroxymonosulfate (PMS) salts.[76] Unlike Fenton system, AOPs adopting persulfate (referred to as PMS and PDS) as peroxide demonstrate many advantages, such as high ROS productivity, less dependence on reaction environment, and lower cost on transport and storage of persulfate salts.[77] Moreover, another advantage of persulfate-based AOPs is the abundant activation approaches. To date, a variety of activation techniques including physical and chemical methods can be applied to activate persulfate to produce sulfate radicals. For example, the activation can be realized by utilizing reduced TM ions, metal oxides, carbonaceous materials, alkaline, heat, and UV light as displayed in **Figure 4**a.[78] The persulfate decomposition and $SO_4^{\bullet-}$ evolution by the means of peroxide bond (O—O) cleavage over these activation methods can be conclusively summarized in Figure 4b, which are classified by the energy input or catalyst-mediated charge transfer.[77]

The intrinsic differences for these $SO_4^{\bullet-}$-based systems in organic component oxidation are the selectivity and oxidation pathways towards these organics with different chemical surroundings. Kim's group systematically explained the causes of such selectivity, which can be traced back to the effects of the functional groups of the organic components.[77] Since the first step of $SO_4^{\bullet-}$-based oxidation process is hydrogen abstraction for saturated hydrocarbons oxidation, the reaction kinetics strongly depend on the nature of functional groups, where the α-H is more prone to be deprived by $SO_4^{\bullet-}$ in the presence of electron-donating groups in these alkanes and aliphatic alcohols, thus resulting in significantly higher reaction kinetics. However, the corresponding reaction kinetics between $^{\bullet}OH$ and saturated hydrocarbons are more stable as the $^{\bullet}OH$ is less susceptible to the chemical surroundings. With respect to the aliphatic carboxylic acids oxidation, the $SO_4^{\bullet-}$-based system undergoes electron-abstraction from the oxygen of carboxyl groups while hydrogen abstraction is the dominant process for $^{\bullet}OH$. This distinguishes the $SO_4^{\bullet-}$-based system from $^{\bullet}OH$-based system.

2.2.4. Catalytic Ozonation

Ozone is an oxidative reagent with the potential of 2.07 V (versus SHE) and has wide applications related to oxidation processes. As one of the broadly used AOPs in wastewater treatment, ozonation is advantageous in terms of cleanness, low cost, and more feasible operation than others.[79,80] Generally,
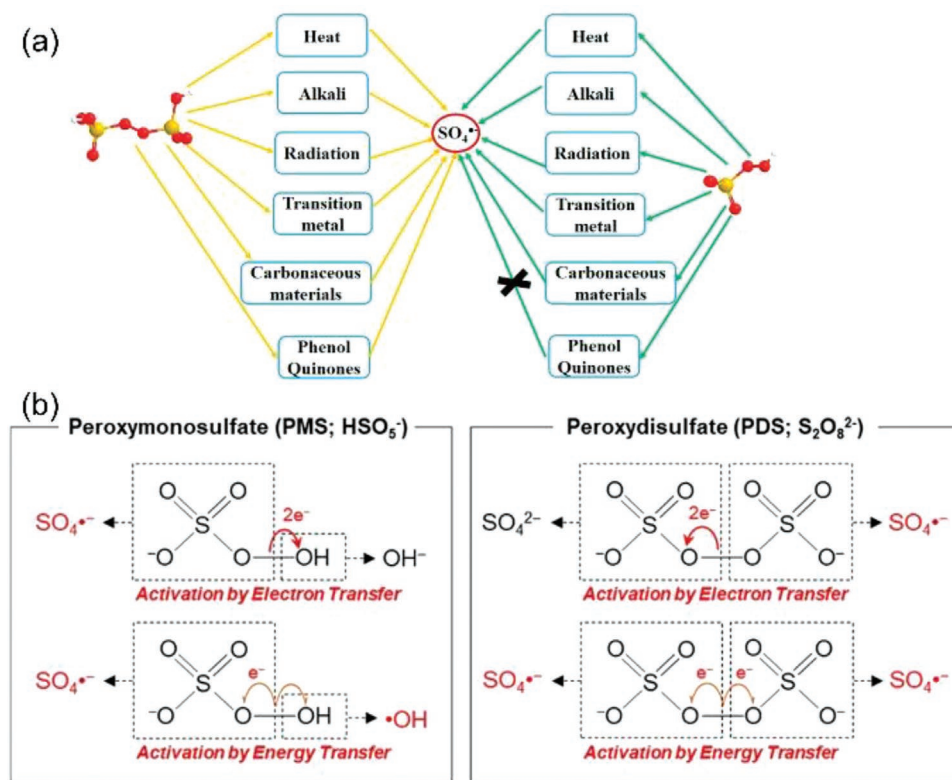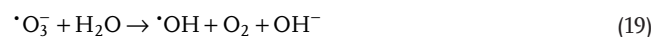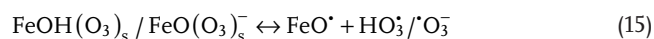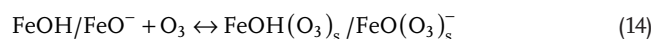

Figure 4. a) Persulfate activation ways. Reproduced with permission.[78] Copyright 2017, Elsevier. b) Persulfate decomposition ways for sulfate radicals generation. Reproduced with permission.[77] Copyright 2020, American Chemical Society.

**ADVANCED
SCIENCE NEWS**
www.advancedsciencenews.com

**ADVANCED
FUNCTIONAL
MATERIALS**
www.afm-journal.de

harmful substance degradation by ozonation mainly includes two mechanisms. One is the direct ozonation, that is, the ozone molecule with high oxidative potential to oxidize the organics directly. Another pathway named indirect oxidation is related to the decomposition of ozone molecules and the generated ·OH with higher oxidation potential can attack the organics.[81–83] Nevertheless, direct ozonation method frequently cannot completely decompose the pollutants resulting in low utilization efficiency and high energy consumption. Alternatively, indirect ozonation provides a promising technique for wastewater treatment.

Similar to Fenton-like reaction, catalysts used for the heterogeneous ozonation could be recycled thus reducing the secondary contamination and material cost. Heterogeneous ozonation can also promote ozone adsorption, dissolution, and decomposition by generating more ·OH, which can overcome the shortcomings of sole ozonation, such as low ozone utilization or selective oxidation.[79,84,85] For instance, goethite or Fe-based materials can be used as heterogeneous catalysts to boost the generation of hydroxyl radicals and improve the catalytic ozonation performance.[84] The possible radical evolution pathway is shown in Equations (14–19) starting from the ozone adsorption on catalyst surface followed by surface complex redox reactions via electron transfer for radicals generation.[86]

$$FeOH/FeO^- + O_3 \leftrightarrow FeOH(O_3)_s / FeO(O_3)_s^- \tag{14}$$

$$FeOH(O_3)_s / FeO(O_3)_s^- \leftrightarrow FeO^\bullet + HO_3^\bullet / {}^\bullet O_3^- \tag{15}$$

$$FeO^\bullet + H_2O \rightarrow FeOH + {}^\bullet OH \tag{16}$$

$$HO_3^\bullet \leftrightarrow {}^\bullet O_3^- + H^+ \tag{17}$$

$$HO_3^\bullet \leftrightarrow {}^\bullet OH + O_2 \tag{18}$$

$${}^\bullet O_3^- + H_2O \rightarrow {}^\bullet OH + O_2 + OH^- \tag{19}$$

2.2.5. O₂ Activation Processes

Abundant O_2 is naturally available from ambient environment. Attempts have been made to activate oxygen to oxidize organic compounds.[87] Oxygen activation can be achieved by heating under high pressure (CWAO), photocatalysis, or catalytic oxidation in dark conditions.[88]

CWAO is proceeded over the heterogeneous catalysts under high temperature (80–250 °C) and pressure (1–50 bar), usually used for the degradation of refractory organic contaminants.[89] CWAO process takes advantage of complete mineralization, high efficiency, and reduced secondary contamination. In this process, oxygen from air can be activated to produce ROS to attack the organic compounds. Catalysts used for CWAO include homogeneous Fe^{2+} (Mn^{2+} or Cu^{2+}), noble metals (Pt, Pd, Ru, or Rh), metal oxides, and perovskites.[90]

To pursue a cost-effective degradation approach, catalytic oxidation under dark and ambient conditions without external

stimulation is also investigated. Although this process shows the merits of low cost and simplicity in reaction system design, the biggest challenge is the low efficiency for contamination elimination. Oxygen activation without energy input is relying on the electron transfer process over catalyst. Electrons from organics play a significant role in the process. Nevertheless, electrons donated by organic molecules are limited restricting the reactive species production rate and pollutants degradation. Perovskites show great potential for oxygen activation under dark condition without the aid of other energy input.[88,91]

3. Recent Progress of Perovskite Oxide in AOPs

3.1. Perovskite Oxides in Fenton-Like System

Dissolved Fe^{2+} ions are known as the classic homogeneous Fenton catalysts suffering drawbacks of sludge generation and narrow working pH range though with announced efficiency.[71] To overcome these disadvantages brought by homogeneous Fenton reaction, plenty of studies are focused on developing heterogeneous catalysts utilizing the iron or other TM-based perovskite oxides, such as $BiFeO_3$, $LaFeO_3$, $LaTiO_3$, and their derivates.[92–95] In this subsection, the progress of heterogeneous perovskite oxide catalysts for hetero-Fenton system is reviewed and the design guidelines to boost the catalytic activity are explained. The hetero-Fenton catalytic activities of selected perovskites are listed in **Table 1**.

3.1.1. Controlling Surface Properties

In 2010, magnetic $BiFeO_3$ nanomaterial synthesized by Luo et al. as Fenton-like catalyst exhibited strong H_2O_2 activation and ·OH production abilities, as well as superior stability under wide pH region.[92] Accelerated H_2O_2 decomposing and ·OH evolution through surface complex formation between H_2O_2 and Fe^{3+} accounted for the notable activity.[92,95] Later, another study by Nie et al. also confirmed that the surface complex formed by the chemisorbed H_2O_2 over $LaFeO_3$ significantly influences the chemical environment, thus weakening the O—O bond and accelerating the Fe^{2+}/Fe^{3+} redox process.[96] Then, to strengthen surface interactions, in situ surface modifying strategy over $BiFeO_3$ via proper organic chelating agents, like tartaric, formic acid, and ethylenediaminetetraacetic acid (EDTA), has been evaluated in $H_2O_2/BiFeO_3$ system.[93] EDTA molecules have high preference to chelate with surface Fe of $BiFeO_3$ via carboxyl groups and thus form steric caves on the surface with a volume of about 94.1 Å³ due to its spatial structure. One large cave could confine two H_2O_2 molecules and thus lead to the increased local H_2O_2 concentration, which promotes the encounter frequency and intensive interactions between active Fe-sites and H_2O_2 molecules. In addition to the physical advantage of H_2O_2 storage led by the confined space, hydrogen bonding between the H of confined H_2O_2 and N as well as carboxyl groups of EDTA would efficiently reduce the charge density of O—O bond and subsequently contribute to the decomposition of H_2O_2 to ROS. Therefore, an enhancing

Table 1. Catalytic activity of various perovskite oxide-based catalysts in Fenton-like system.

Materials	Organic pollutants	Catalyst dosage	H_2O_2 dosage	Degradation rate	Metal leaching (B-site)	Main ROS	Ref.
$LaTi_{0.4}Cu_{0.6}O_3$	Rhodamine B (RhB) [8 ppm]	1.4 g L^{-1}	20 m$_M$	94.0% at 120 min	Cu: 1.4 ppm at pH 4.4	$^·OH$, $HO_2^·$	[48]
$BiFeO_3$	RhB [10 μ$_M$]	0.5 g L^{-1}	10 m$_M$	95.2% at 90 min	0.498 ppm	$^·OH$	[92]
$BiFeO_3$/EDTA	BPA [0.1 m$_M$]	0.5 g L^{-1}	10 m$_M$	91.2% at 120 min	0.98 ppm	$^·OH$	[93]
$LaFeO_3$/SBA-15	RhB [0.02 m$_M$]	2.0 g L^{-1}	6 mL L^{-1}	100% at 120 min	–	–	[94]
$LaFeO_3$	Sulfamethoxazole [3 ppm]	1.4 g L^{-1}	23 m$_M$	100% at 120 min	0 ppm	$^·OH$	[96]
$La_{1.15}FeO_3$	Methyl orange [5 ppm]	0.5 g L^{-1}	0.198 $_M$	100% at 80 min	0.785 ppm	$^1O_2$, $^·OH$	[97]
$BiFeO_3$	RhB [30 ppm]	1.0 g L^{-1}	44 ppm	>90% at 6 min	–	$^·OH$	[102]
Pb-$BiFeO_3$/rGO	Perfluorooctanoic acid [50 ppm]	1.0 g L^{-1}	44 ppm	90% at 5 min	–	$^·OH$	[103]
$BiFe_{0.8}Cu_{0.2}O_3$	Phenol [10 ppm]	0.5 g L^{-1}	10 m$_M$	91% at 120 min	Cu: 0.79 ppm Fe: 0.029 ppm	$^·OH$	[104]
$LaMn_{0.4}Fe_{0.6}O_3$	Methyl blue (MB) [15 ppm]	20 μg L^{-1}	0.6 mL L^{-1}	98.0% at 140 min	–	–	[105]
$LaAl_{0.95}Cu_{0.05}O_3$	2-Chlorophenol [10 ppm]	1.0 g L^{-1}	10 m$_M$	100% at 120 min	0.523 ppm	$^·OH$	[107]

bisphenol A (BPA) degradation efficiency and boosting $^·OH$ formation capacity were achieved. Newly different strategy was proposed by Li et al. to fine tune surface properties by nano-compositing inert oxide with perovskite oxides.[97] Benefiting from the inert La_2O_3 compositing, a series of surface phys-icochemical properties of $La_{1.15}FeO_3$ have been tuned towards developing superior catalytic activity (**Figure 5**a–d), such as improved surface defects content, lower oxidation states of B-site Fe, H_2O_2 adsorption ability, electron delivery rate, higher zeta potential, and positively charged surface. Moreover, a more stable cubic crystal structure was attained with high resistance

against leaching. All of the above features favor the H_2O_2 acti-vation process. Inspired by this, to overcome the drawback of the unsatisfactory electrical conductivity, future attention may be paid to the advanced exsolution or self-assembly technolo-gies to construct active hybrids with multiple integrated func-tions for AOPs, such as in situ exsolved metal nanoparticles/perovskite composites and multi-phase perovskites via phase segregation.

Surface area is considered as a key factor for catalytic process since high surface area would offer a large quantity of adsorp-tion sites and catalytically active sites. However, low specific
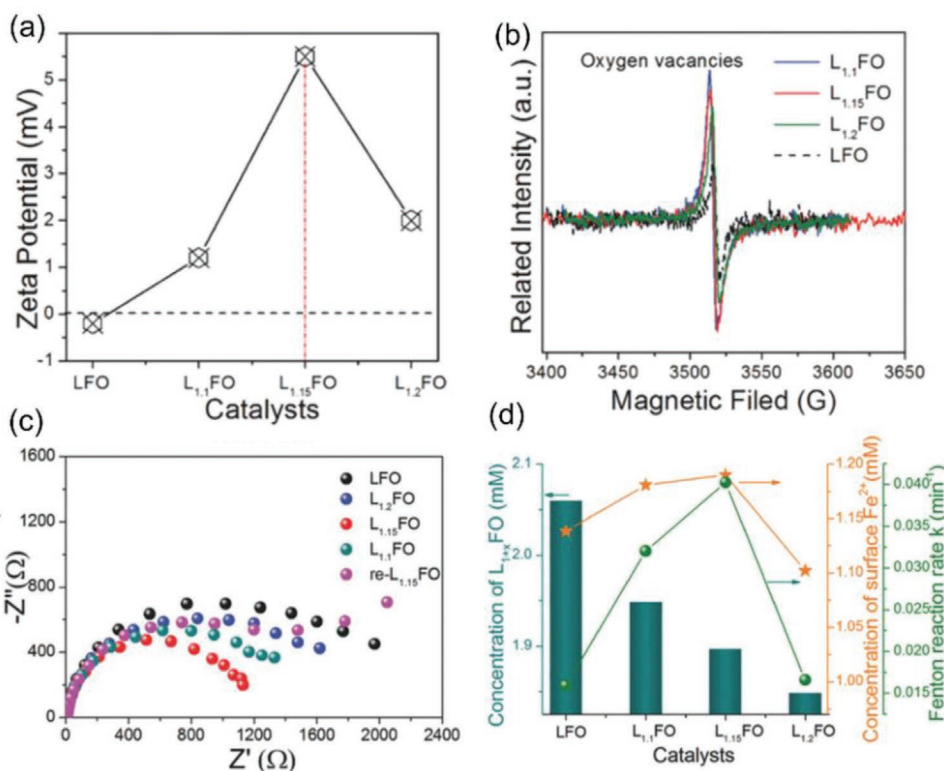
Figure 5. The physicochemical properties of $La_{1+x}FeO_3$: a) Zeta potential at pH 7; b) Oxygen vacancy content; c) Nyquist plot; and d) Correlation between Fenton-like reaction kinetics and Fe^{2+} concentration of $La_{1+x}FeO_3$. Reproduced with permission.[97] Copyright 2018, Wiley-VCH.

surface area and small pore volume are usually encountered for these perovskite oxides prepared under high temperature. Efforts have been made to minimize this drawback using a series of synthesis methods and post-treatments, like template methods, microwave-assisted techniques, and hetero-conjunction.[94,98–101] For instance, nanoscaled $LaFeO_3$ perovskite oxide particles supported on high surface area zeolite SBA-15 would yield catalysts with high specific surface area and show significantly improved Fenton activity.[94] Besides, carbon aerogel supported $BiFeO_3$ nanocatalyst was prepared via sol-gel method with considerably higher surface area (404 m^2 g^{-1}) than the pristine $BiFeO_3$ (14 m^2 g^{-1}), exhibiting efficient ketoprofen removal and mineralization ability. About 60% TOC removal was attained in 300 min for the hybrid catalyst, while only a 15% mineralization was achieved for bulk $BiFeO_3$.[100] Microwave-assisted hydrothermal preparation method as an alternative approach enabled $BiFeO_3$ and Pb-doped $BiFeO_3$/rGO composite with relatively high surface area (78.51 and ≈84.2 m^2 g^{-1}, respectively) in contrast to the conventional hydrothermal and sol-gel ways.[102,103] In addition to the benefits given by high surface area, another factor that contributed to the superior catalytic Fenton activity is the enhanced crystallinity of $BiFeO_3$ structure prepared by the microwave-assisted method.

3.1.2. Bulk Composition Tailoring

The decisive factor of ABO_3-type perovskite oxides for H_2O_2 catalytic activation is the valence alternation of B-site TMs to form active redox couple, facilitating the charge transfer from catalyst to H_2O_2 for O—O bond breaking and ROS evolution. Doping provides an appealing approach for scalable control of B-site oxidation states. For example, the introduction of Cu into $LaTiO_3$ can result in the coexistence of Ti^{3+}/Ti^{4+} and Cu^+/Cu^{2+} rather than a single oxidation state of Ti^{3+} in parent $LaTiO_3$, which served as redox couples for delivering electrons to activate O-O bond in H_2O_2.[48] Miao et al. also manifested that Fe^{2+} formation in lattice and Fe^{2+}/Fe^{3+} redox cycle are more prone to be mediated by introducing Cu into $BiFeO_3$ lattice.[104]

Besides, defects engineering was pursued over decades since its indispensable contribution to catalytic performance. Aliovalent doping strategy offered the Cu-doped $LaTiO_3$ with a considerable amount of surface oxygen defects known as the strong active sites for peroxide adsorption and activation. The enhancement of anion and cation dyes decomposition was also observed over Mn-doped $LaFeO_3$ catalytic hetero-Fenton reaction.[105] Furthermore, Cu stabilization in lattice and exposure of high surface Cu^+/Cu^{2+} content in Mn-incorporated $LaCuO_3$ are additional advantages accounted for the optimized Fenton activity.[106] Wang et al. conveyed that incorporating of only 5% mol. Cu into $LaAlO_3$ would lead to significant positive effects on activity and stability due to the optimization of the electron structure.[107] The higher electronegativity of Cu than La and Al would localize the electrons and form electron-rich Cu center, promoting the reduction of H_2O_2 to $\cdot OH$ via electron migration. Apart from the electron-rich Cu center, oxygen vacancies also enhanced the radicals generation via H_2O_2 and H_2O dissociation.

3.2. Perovskite Oxides in Photo/Photo-Fenton Reactions

Recently, perovskite oxide semiconductors as photocatalysts have attracted tremendous attention for potentials in energy conversion and environmental remediation. The key factors of photocatalysts are the capacity of absorption solar energy to generate electron-hole pairs and the ability to suppress the recombination rate of electron-hole pairs.[75] This subsection will elucidate the working principles and summarize the recent progress in minimizing bandgap energy (E_{bg}) and improving charge separation ability of perovskite oxides for photo/photo-Fenton system.

3.2.1. Band Gap Engineering

A- and O-Site Elements Selection and Doping: Fe-containing perovskite oxides, such as bismuth ferrite ($BiFeO_3$) and lanthanum ferrite ($LaFeO_3$), are of considerable interest in photocatalysis because of their narrowed bandgap (2.0–2.7 eV), high visible-photo adsorption capacity, low toxicity, and strong stability.[108–110] For further activity improvement, the high design flexibility of ABO_3 seems to find its niche in optimizing the compositions by partially or fully substitution at either A/B/O-site with foreign dopants. For example, Li et al. examined the effect of A-site rare-earth element of $LnFeO_3$ (Ln = Pr and Y) on their photocatalytic activities.[111] The $PrFeO_3$ gave a better photocatalytic activity than $YFeO_3$ as the former exhibited slightly reduced bandgap energy (2.46 versus 2.52 eV). A series of Ca-doped $La_{1-x}Ca_xFeO_3$[112] and Ba-doped $Bi_{1-x}Ba_xFeO_3$[113] had also been prepared via reverse microemulsion and sol-gel methods, respectively, for organic pollutants oxidation under visible light. It was found that the incorporation of ≈10% mol. The optimum amount of Ca and Ba into the lattice led to the best photodegradation performance but further higher level doping (>10%) would retard the activity. The partial substitution of trivalent A-site cations with divalent Ca or Ba could decrease the crystal size and increase the specific surface area, which plays the key roles in enhancing both the photo and organic molecules adsorption. Moreover, the Ca dopants acting as donor center could increase the number of photo-induced electrons, thus resulting in pronounced photo-activity.

Owing to the merit of higher 2p orbital potential energy of N than O, N doping at O-site can effectively shift the VB upward without influencing the CB.[114] In light of this, N-doped $LaFeO_3$ coupled with TiO_2 was successfully prepared for photocatalytic removal of organics.[115] As expected, a narrow bandgap of ≈1.82 eV was achieved compared to the pristine 2 eV of $LaFeO_3$ due to an upward shift of VB, thus improving the visible-photo adsorption (**Figure 6**a,b). Later, Rao and his co-workers used hydrothermal method to embed N into $KTaO_3$ and yielded a high doping level (5.20 at%) N-$KTaO_3$.[116] Hence a dramatically decreased E_{bg} of N-$KTaO_3$ was calculated to be 2.54 eV compared to 3.53 eV of the pristine $KTaO_3$ due to the hybrid VB (N 2p and O 2p orbitals), where the enhanced visible-light adsorption induced by the narrowed band gap mainly accounts for the good photocatalytic activity. Recently, another study demonstrates that the Fermi level of $BiFeO_3$ would be shifted towards the CB by partially substituting lattice O with N.[117] Calculation
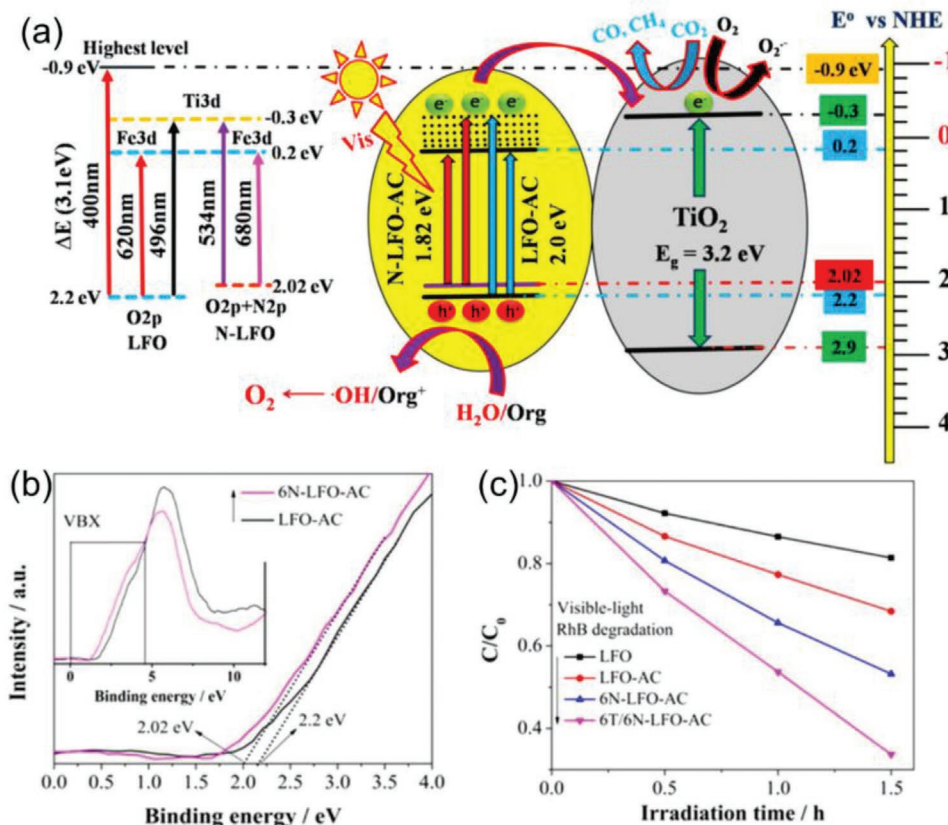
Figure 6. a) Schematic illustration of band structure and photocatalytic process over N-doped $LaFeO_3$/TiO_2 composite. b) VB position of N-doped and undoped $LaFeO_3$. c) Photocatalytic Rhodamine B degradation over pristine $LaFeO_3$ (LFO), aminofunctionalized carbon-templated porous $LaFeO_3$ (LFO-AC), N-doped LFO-AC (6N-LFO-AC), and TiO_2-coupled 6N-LFO-AC (6T/6N-LFO-AC). Reproduced with permission.[115] Copyright 2016, American Chemical Society.

results show that with the existence of N at O-site, the 2p orbitals of N and O would overlap with Fe 3d orbitals near the Fermi level; as a result of which, the bandgap could be reduced from 2.16 to 1.71 eV, thus enhancing visible-light adsorption.

B-Site Cation Selection and Doping: Reduction of E_{bg} can also be performed through the approach of B-site element partial substitution. For instance, the Ru-doped $LaFeO_3$ coupled with Fe_2O_3 exhibited high efficiency towards photo-Fenton system.[118] Due to the benefits of a narrowed bandgap of 1.85 eV, complete TOC removal of 280 mg L^{-1} was attained within 75 min under visible light illumination and 38 mmol L^{-1} H_2O_2. Phan and co-workers prepared Cu-doped $LaFeO_3$ to evaluate the photo-Fenton activities and observed that the partial substitution could give rise to a certain amount of oxygen defects and decreased E_{bg} value (2.29 eV).[119]

In addition to the sole doping process, Wang et al. adopted a dual-doping strategy by introducing Ag and Nb into A- and B-site, respectively, to fabricate $Ag_{0.75}Sr_{0.25}Nb_{0.75}Ti_{0.25}O_3$.[120] The hybridized VB (Ag 4d + O 2p) of the prepared perovskite semiconductor was shifted towards a more negative position due to the involvement of Ag 4d orbitals, while the CB (Ti 3d + Nb 4d) moved to a more positive position because of the higher potential of Nb 4d than Ti 3d. Thus the partial substitution of both A- and B-site elements yielded a decreased bandgap (2.8 eV) versus 3.2 eV of $SrTiO_3$. The $Ag_{0.75}Sr_{0.25}Nb_{0.75}Ti_{0.25}O_3$ with such

a modulated band structure exhibited significantly improved photocatalytic oxidation of acetaldehyde and 2-propanol under visible-light irradiation. Besides, the narrowed bandgap energy (1.87 eV) of $Bi_{0.97}Ba_{0.03}Fe_{0.9}Cu_{0.1}O_3$ was noticeably attained as a result of Ba and Cu co-doping.[121] Upon visible-light irradiation, the lowered E_{bg} benefits the photo-Fenton catalytic activity and a complete 2-chlorophenol (2-CP, 50 ppm) removal was achieved in 70 min, much faster than $BiFeO_3$ as only 20% removal was attained at similar conditions. Vanga and co-workers also proved that Nd and Ni co-doping could reduce E_{bg} and show better performance due to the alternation of lattice parameters of $BiFeO_3$ by hetero-doping.[122]

Surface Engineering: In situ surface modification over $BiFeO_3$ nanoparticles by employing organic ligands (EDTA) greatly boosted the photo/photo-Fenton catalytic efficiency.[123] With trace amount of EDTA (0.4 m_M) in photo/$BiFeO_3$/H_2O_2 system, a 128-fold improvement of pseudo first-order rate constant (i.e., 1.30 to 0.0101 min^{-1}) was attained. Such notable enhancement can be mainly ascribed to the improved visible light response because of the lower E_{bg} (1.80 eV) of EDTA-modified $BiFeO_3$, which is 2.10 eV for the pristine $BiFeO_3$ nanoparticles. With the enhanced visible photo adsorption capacity, more photo-excited electrons would be produced and captured by the H_2O_2 to produce ·OH directly.[124] Meanwhile, the surface EDTA ligand could also accept photo-charges to produce intermediate free

ADVANCED
SCIENCE NEWS
www.advancedsciencenews.com

ADVANCED
FUNCTIONAL
MATERIALS
www.afm-journal.de

radicals, which would activate dissolved O_2 for further ·OH generation.

3.2.2. Separating Photo-Induced Electron-Hole Pairs

A- and O-Site Doping: Generally, hetero-doping either at cation-sites or O-site can cause various effects on multiple features of perovskite oxides. The N-dopant at O-site demonstrates great potential to enhance photocatalytic activity by reducing E_{bg}. Additionally, another important factor, the separation ability of photo-induced electron-hole pairs, could also be impacted by N-dopant. A recent study shows that composite semiconductor (N-doped porous $LaFeO_3$ and TiO_2) with reduced bandgap (≈1.82 eV) and superior charge separation capacity presented superior optical photocatalytic performance for 2,4-dichlorophenol (2,4-DCP) removal.[115] A threefold improvement for the degradation efficiency to pristine $LaFeO_3$ was observed (Figure 6c), which is ascribed not only to the narrow bandgap and extended adsorption of visible light, but also the N-doping induced surface state favored the photo-induced holes trapping and thus suppressed the electron-hole recombination rate. As a result, visible-photo induced holes as the powerful oxidant oxidizing H_2O to generate high amounts of ·OH to attack contaminant molecules.

In addition to the N at O-site, rare earth (RE) dopants at A-site may also cause positive influence on charge carrier separation. Guo et al. observed that $Bi_{0.9}Gd_{0.1}FeO_3$ exhibited superior photocatalytic activity to $BiFeO_3$ as the former has much faster Rhodamine B (RhB) removal efficiency under visible light.[125] Further analysis was conducted for seeking the potential factors. Intriguingly, comparing to undoped $BiFeO_3$, a blue shift of $Bi_{0.9}Gd_{0.1}FeO_3$ adsorption spectra was found, thus giving an even increased bandgap (from 2.03 to 2.2 eV), which means other factors with more contribution. A similar phenomenon was observed in $BiREWO_6$ (RE = La, Pr, Gd, and Dy), where the $BiGdWO_6$ with even higher E_{bg} showed a fast organic removal rate.[126] The reasonable explanation is that due to the phase transition from rhombohedral to a more symmetrical orthorhombic phase structure with the Gd-dopant, the increased dielectric constant is the key factor as the high dielectric constant enlarges the space-charge region. As shown in **Figure 7**, the space-charge region is an electron depletion or accumulation area formed near the semiconductor surface when contacting with different phases in gas or liquid. This kind of electron redistribution across the semiconductor relies on the charged states of contacted phase. When the positive/negative charges accumulated on the surface of semiconductor, the band will bend downward/upward as a result of the forming electron accumulation/depletion layer. The sloping energy bands would benefit the electron-hole separation as the most carriers accumulated on the subsurface can be efficiently transported to the surface for reactions. With the increased width of charge-space region led by high dielectric constant, more charge carriers accumulate near the surface and contribute to photocatalytic activity consequently.

Another theory for the enhanced electron-hole pairs separation ability of RE-doped perovskite is related to the electronic configuration of RE dopants as concluded by Li et al.[127] Among
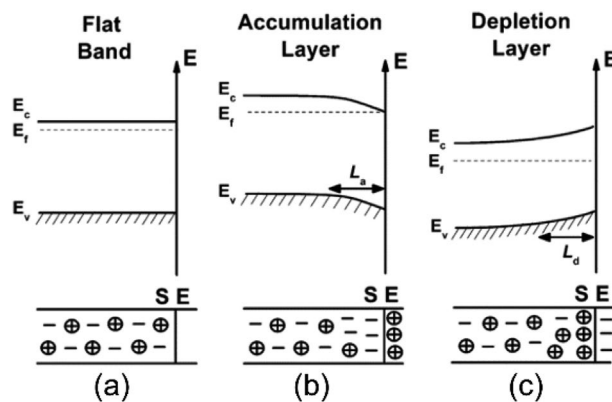
Figure 7. A Schematic depicting of space charge region and band bending structure; S and E refer to semiconductor and electrolyte, respectively. Reproduced with permission.[125] Copyright 2010, American Chemical Society.

La, Pr, Gd, Er RE dopants, Gd-doped $La_{1.5}Gd_{0.5}Ti_2O_7$ nanocrystalline exhibited the best performance towards methyl orange (MO) photodegradation. The proposed mechanism is that the half-filled 4f shell of the Gd^{3+} can promote the electron transfer and thus improve the electron-hole separation efficiency. To be more specific, the half-filled electronic configuration of the f shell for metal ions is more stable and tends to recover to the initial state when such a configuration is destroyed. This unique character favors the electron transfer and charge carrier separation by shallowly trapping electrons. Despite other metal ions can also trap electrons, but the de-trapping process is more difficult than the metal ions with half-filled f shell. Therefore, $La_{1.5}Gd_{0.5}Ti_2O_7$ presents higher efficiency in the electron-hole pair separation.

Phase separation and oxygen deficiency of perovskite oxides by hetero-doping should also be considered. Zaki et al. prepared Ca-doped (Ca > 10%) $Bi_{1-x}Ca_xFeO_3$.[128] A second phase of $\gamma(\alpha)$-Fe_2O_3 was generated and composited with $BiFeO_3$, yielding a p/n heterojunction. The p/n nanojunctions optimized the heterogeneous photo-Fenton activity by prolonging the lifetime of electron-hole pairs activated by visible light. Zhou et al. fabricated $Bi_{0.97}Er_{0.03}FeO_3$ nanoparticles for photocatalytic decomposition of tetracycline hydrochloride under visible light.[129] Through Er doping, a boost visible light response and decreased rate of electron-hole recombination were reached, which can be mainly attributed to the large number of oxygen vacancy formation via doping. Generally, aliovalent or isovalent doping gives rise to a high amount of oxygen vacancy that can trap photo-induced electrons due to its less-electron-rich character.

Heterojunction Construction: Composite construction demonstrates a promising way to overcome the drawbacks of large particle size, low specific surface area, and inferior charge transfer capacity of single-phase perovskite oxide for photocatalytic process.[130,131] For example, a $LaFeO_3$/montmorillonite nanocomposite was synthesized by depositing nano-$LaFeO_3$ on montmorillonite surface.[132] Uniform $LaFeO_3$ nanoparticles (10–15 nm) were immobilized on 2D montmorillonite intimately through Si—O—Fe bonds. Both the uniform nanoparticles and intimate interaction are conducive for photo adsorption and carriers separation. Besides, the property of

abundant hydroxyl groups on the montmorillonite surface plays a vital role in photo-induced holes capture. Upon visible light illumination, the photo-induced holes could be trapped by the surface hydroxyl groups for $\cdot$OH evolution while the excited electrons reacted with dissolved oxygen to generate superoxide radicals ($O_2^{\cdot-}$). As a result, 99.34% of RhB could be efficiently degraded in 90 min, much faster than the bulk $LaFeO_3$.

Recently, carbonaceous materials, like graphene oxide (GO), reduced GO (rGO), graphitic carbon nitride (g-C_3N_4), and carbon spheres, have been selected as candidates for compositing because of their pronounced electron delivery ability, specific 2D structure, and semiconductor properties.[133–139] An et al. introduced GO into the $BiFeO_3$ precursor followed by sintering, yielding a composite of Graphene/$BiFeO_3$ for photo-Fenton reaction.[136] A rapid decomposition of tetrabromobisphenol A (TBBA, 5.43-fold to single $BiFeO_3$) was achieved for GO/$BiFeO_3$, the main cause for which is the enhanced photo-induced charge/hole (e^-/h^+) separating capacity by fast electron delivery from the CB of $BiFeO_3$ to graphene. Graphene could serve as a competitive electron acceptor to deprive photo-induced electrons due to its unique structure of 2D π-conjunction, and thus promoted H_2O_2 activation for $\cdot$OH production. Identical results were observed in the composites of g-C_3N_4/$BiFeO_3$, g-C_3N_4/$LaFeO_3$, and rGO/$LaFeO_3$ in photo-Fenton system and photocatalytic degradation process.[133,134,138,140] The enhancement of optical light adsorption and suppressed recombination of charge carriers due to fast electron migration contribute to the improved photocatalytic activities. This is good evidence that the integration of carbon with perovskite oxides can enhance the charge carriers separation ability. However, due to the difficulty in maintaining perovskite skelton during the chemical compositing process with carbon materials, the existing fabrication methods are still

based on the classical physical approaches by mixing the as-prepared individual compounds. Thus, in order to prepare such composites with intimate interaction, more advanced chemical methods should be developed. Moreover, considering the variety of advantages of 2D nanomaterials, like the unique electronic property, large specific surface area, and short charge diffusion path, rational design of 2D/2D heterojunction would theoretically enhance the photocatalytic performance. For example, D–J type of layered perovskite oxides ($KCa_2Nb_3O_{10}$) was exfoliated into ultrathin nanosheets, which coupled with g-C_3N_4 (**Figure 8**a,b) via hydrothermal approach and exhibited notable improvement of visible photocatalytic efficiency for pollutant oxidation than each of single component.[137] Because of the intimate interface and accelerated interfacial charge transfer, the enhancement of suppression ability of photo-excited electron-hole recombination contributes to the superior activity (Figure 8c,d). In addition to the carbon materials, novel 2D/2D layered heterojunctions containing P-$La_2Ti_2O_7$ and Bi_2WO_6 were proposed by researchers.[141] Because the conduction and VBs of Bi_2WO_6 are more positive than P-$La_2Ti_2O_7$, a type-II binary heterojunction was formed with the huge potential difference in the composite energy band, which expedites the electron transfer. The compact interaction of composite provides unique fast charge transfer nanochannels and thus efficiently facilitates the electron-hole pairs separation. A Z-scheme heterojunction of low dimensional Ag_2S coupled with $BiFeO_3$ was applied as photo-Fenton catalysts under visible light illumination for MO oxidation.[142] With an optimal content of 15% Ag_2S in composite, a noticeable enhancement in photocatalytic activities was observed as shown in **Figure 9** and **Table 2**. Comparing to pristine $BiFeO_3$, the enhanced photocurrent, lower charge transfer resistance, and decreased photoluminescence peak at $\approx$520 nm indicated superior photo excited e^--h^+ separation
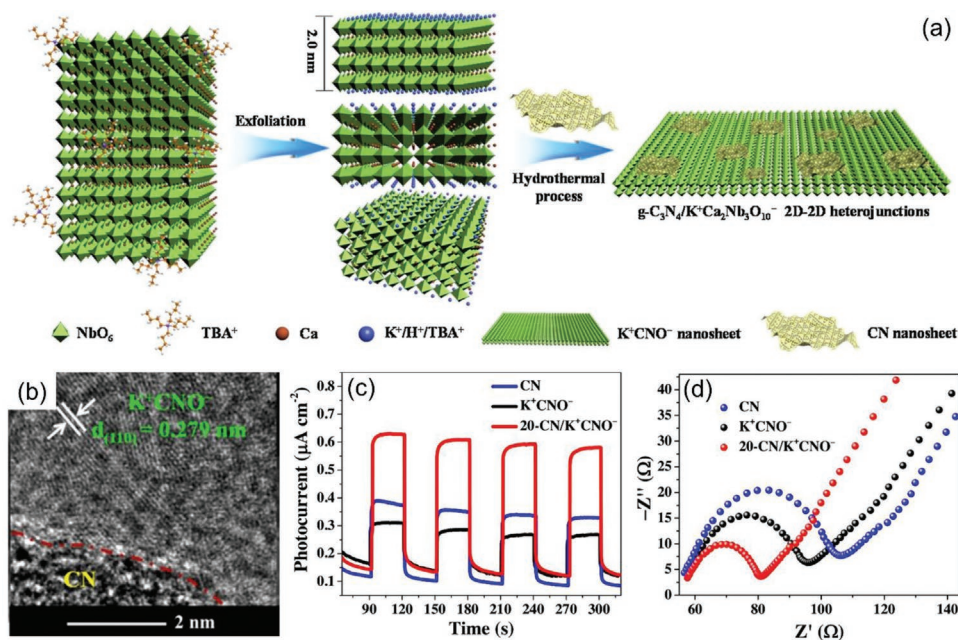
Figure 8. a) Schematic illustration of perovskite exfoliation and compositing with g-C_3N_4. b) HRTEM image of g-C_3N_4/$KCa_2Nb_3O_{10}$ (CN/KCNO) heterojunction. c) Transient photocurrent response and d) Nyquist plot of CN/KCNO, CN, and KCNO. Reproduced with permission.[137] Copyright 2017, Wiley-VCH.
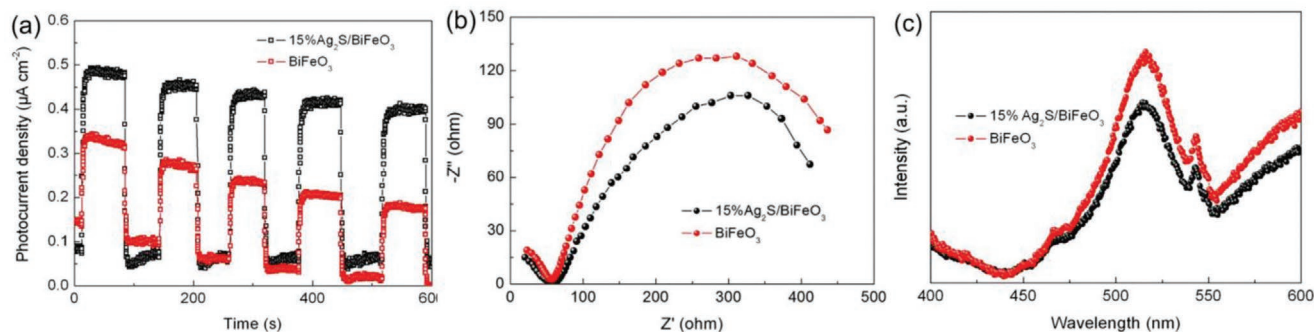
Figure 9. a) Transient photocurrent, b) Nyquist plot, and c) Photoluminescence spectra of $BiFeO_3$ and $Ag_2S/BiFeO_3$ composite, respectively. Reproduced with permission.[142] Copyright 2019, MDPI.

property of $Ag_2S/BiFeO_3$ composite. This led to a 3.5-fold increment of the rate constant versus the sole $BiFeO_3$. Moreover, the composite of $BaTiO_3$ and hemin was designed to be in a highly conjugated structure, where a chemical interaction was established. Surface carboxylate group integrated the hemin and $BaTiO_3$ chemically via C—O—Ti bonds and thus initiated the electronic coupling among π^* orbitals of hemin and 3d orbitals of Ti. Because of this bridging, non-photo-induced electron transfer was enhanced to change the composite from singlet to triplet states and hindered the recombination consequently.

3.3. Perovskite Oxides in Peroxymonosulfate Activation Process

As discussed previously, compared with other radicals, highly oxidative sulfate radicals with the oxidative potential of 2.5–3.1 V (versus SHE) and longer half-life (30–40 ms) demonstrate promising potential to turn refractory organics into carbon oxide.[76,143] Peroxymonosulfate salts are prone to be activated conducting over either homogeneous or heterogeneous

catalysts to generate free radicals and non-radicals, such as sulfate radicals, hydroxyl radicals, superoxide radicals, and singlet oxygen.[144] The perovskite-based PMS activation reaction mechanisms and design protocols of perovskite oxides for PMS excitation will be discussed in this section, including composition tailoring (i.e., A/B-site elements adjusting and doping), defects engineering, surface properties, and morphology control. Some representative outcomes have been compiled in **Table 3**.

3.3.1. Bulk Composition Tailoring

B-Site Elements Selection and Doping: B-site TM cations with variable oxidation states can form redox couples to facilitate the electron transfer for catalytic reaction. Lin et al. evaluated the catalytic activity of various transition elements (Co, Cu, Fe, and Ni) in B-site on PMS activation and dye decomposition.[145] $LaCoO_3$ presented the highest activity followed by $LaCuO_3$ and $LaNiO_3$, where $LaFeO_3$ showed inferior performance in RhB degradation.

Table 2. Photo/photo-Fenton catalytic degradation performance of selected perovskite oxide-based semiconductors.
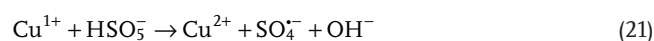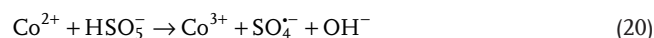
Materials	E_{bg} [eV]	Organic pollutants	Catalyst dosage	Light type	H_2O_2	Degradation rate	Main radicals	Ref.
$Bi_{0.88}Ba_{0.12}FeO_3$	–	Toluene [100 ppm]	0.4 g L^{-1}	$\lambda > 400$ nm	0.6 m$_M$	98% at 45 min	·OH, O$_2$·$^-$	[113]
N-doped $LaFeO_3/TiO_2$	1.82	2,4-DCP [10 ppm]	0.25 g L^{-1}	$\lambda > 420$ nm	–	65% at 1.5 h	·OH	[115]
N-doped $KTaO_3$	2.54	MB [0.01 m$_M$]	0.2 g L^{-1}	visible light	–	98.6% at 6 h	·OH, O$_2$·$^-$, HOO·	[116]
N-doped $BiFeO_3$	1.71	BPA [25 ppm]	1 g L^{-1}	Visible light	10 m$_M$	60% at 2 h	·OH, O$_2$·$^-$, h$^+$, HO$_2$·	[117]
$Ag_{0.75}Sr_{0.25}Nb_{0.75}Ti_{0.25}O_3$	2.8	Acetaldehyde [300 ppm]	0.8 mg L^{-1}	$\lambda > 420$ nm	–	100% at 200 min	·OH, O$_2$·$^-$, h$^+$	[120]
$Bi_{0.97}Ba_{0.03}Fe_{0.9}Cu_{0.1}O_3$	1.87	2-CP [50 ppm]	0.4 g L^{-1}	$\lambda > 400$ nm	10 m$_M$	73% at 70 min	·OH	[121]
$BiFeO_3$-EDTA	1.80	Phenol [3 m$_M$]	0.5 g L^{-1}	$\lambda > 420$ nm	60 m$_M$	90% at 2.5 h	·OH	[123]
$Bi_{0.9}Gd_{0.1}FeO_3$	2.2	RhB [5 ppm]	1 g L^{-1}	$\lambda > 420$ nm	–	94% at 2 h	·OH	[125]
$BiREWO_6$	2.46	MB [0.01 m$_M$]	1 g L^{-1}	visible light	–	92% at 3 h	·OH, O$_2$·$^-$, h$^+$	[126]
$Bi_{0.97}Er_{0.03}FeO_3$	2.16	TCH [30 ppm]	2 g L^{-1}	$\lambda > 420$ nm	–	75.8% at 3 h	O$_2$·$^-$, h$^+$	[129]
$LaFeO_3$/montmorillonite	2.24	RhB [0.02 m$_M$]	1 g L^{-1}	$\lambda > 400$ nm	–	99.34% at 1.5 h	·OH, O$_2$·$^-$	[132]
g-$C_3N_4/BiFeO_3$	≈1.4	Guaiacol	0.5 g L^{-1}	$\lambda > 420$ nm	15 m$_M$	100% at 60 min	·OH	[133]
Graphene/$BiFeO_3$	1.0	TBBA [0.02 m$_M$]	0.5 g L^{-1}	$\lambda > 420$ nm	20 m$_M$	80% at 15 min	·OH	[136]
g-$C_3N_4/KCa_2Nb_3O_{10}$	2.71/3.38	TCH [35 ppm]	4 g L^{-1}	$\lambda > 400$ nm	–	81% at 1.5 h	O$_2$·$^-$, h$^+$	[137]
P-$La_2Ti_2O_7/Bi_2WO_6$	2.86/2.47	RhB [10 ppm]	1 g L^{-1}	$\lambda > 420$ nm	–	99.02% at 80 min	O$_2$·$^-$	[141]
$Ag_2S/BiFeO_3$	2.15	MO [5 ppm]	0.6 g L^{-1}	$\lambda > 420$ nm	2 m$_M$	≈100% at 4 h	·OH, O$_2$·$^-$, h$^+$	[142]

ADVANCED
SCIENCE NEWS
www.advancedsciencenews.com

ADVANCED
FUNCTIONAL
MATERIALS
www.afm-journal.de

Table 3. Catalytic activity of selected perovskite oxide-based catalysts for PMS-based AOPs.

Catalyst	Organic pollutants	Catalysts dosage	PMS dosage	Degradation rate	TOC removal	Main radicals	Ref.
$PrBaCo_2O_{5+\delta}$	Phenol [20 ppm]	0.1 g L^{-1}	2 g L^{-1}	100% at 15 min	–	$SO_4^{\cdot-}$, $\cdot OH$	[27]
	MB [10 ppm]	0.05 g L^{-1}	0.75 g L^{-1}	100% at 20 min	–		
$LaCo_{0.4}Cu_{0.6}O_3$	Phenol [20 ppm]	0.1 g L^{-1}	0.2 g L^{-1}	99% at 12 min	30% at 1 h	$SO_4^{\cdot-}$	[32]
$SrCo_{1-x}Ti_xO_{3-\delta}$	Phenol [20 ppm]	0.1 g L^{-1}	2 g L^{-1}	100% at 25 min	77% at 5 h	$SO_4^{\cdot-}$, $\cdot OH$	[42]
$LaCo_{0.5}Mn_{0.5}O_{3+\delta}$	Phenol [20 ppm]	0.1 g L^{-1}	2 g L^{-1}	100% at 40 min	67.3% at 5 h	$\cdot OH$	[65]
$LaCoO_3$	RhB [10 ppm]	0.1 g L^{-1}	0.1 g L^{-1}	100% at 60 min	–	$SO_4^{\cdot-}$, $\cdot OH$	[145]
$LaCuO_3$	RhB [10 ppm]	0.1 g L^{-1}	0.1 g L^{-1}	≈50% at 60 min	–		
$LaFeO_3$	RhB [10 ppm]	0.1 g L^{-1}	0.1 g L^{-1}	≈45% at 60 min	–		
$LaNiO_3$	RhB [10 ppm]	0.1 g L^{-1}	0.1 g L^{-1}	≈60% at 60 min	–		
$LaCoO_3$-SiO_2	2-phenyl-5-sul-fonebzimidazole [5 ppm]	0.5 g L^{-1}	5 m$_M$	100% at 30 min	–		[146]
Sr_2CoFeO_6	BPA [20 ppm]	0.45 g L^{-1}	10^{-4} $_M$	100% at 90 min	65% at 6 h	$SO_4^{\cdot-}$	[148]
$SrCoO_3$	Phenol [20 ppm]	0.2 g L^{-1}	10^{-4} $_M$	100% at 2.5 h	68% at 6 h	$SO_4^{\cdot-}$	[149]
$LaCoO_3$	Phenol [20 ppm]	0.2 g L^{-1}	10^{-4} $_M$	95% at 2.5 h	65% at 6 h		
$BaCoO_3$	Phenol [20 ppm]	0.2 g L^{-1}	10^{-4} $_M$	84% at 2.5 h	35% at 6 h		
$CeCoO_3$	Phenol [20 ppm]	0.2 g L^{-1}	10^{-4} $_M$	980 at 2.5 h	32% at 6 h		
$La_{0.4}Sr_{0.6}MnO_{3-\delta}$	Phenol [20 ppm]	0.2 g L^{-1}	2 g L^{-1}	100% at 90 min	–	$^1O_2$	[150]
BSCF	Phenol [20 ppm]	0.1 g L^{-1}	6.5 m$_M$	100% at 30 min	60%	$SO_4^{\cdot-}$, $\cdot OH$	[151]
$LaMnO_3$	Phenol [25 ppm]	0.2 g L^{-1}	0.5 g L^{-1}	≈100% at 30 min	–	$^1O_2$	[153]
$SrCo_{0.6}Ti_{0.4}O_{3-\delta}$ @CoOOH	Phenol [20 ppm]	0.06 g L^{-1}	2 g L^{-1}	≈100% at 20 min	–	$SO_4^{\cdot-}$, $\cdot OH$, $^1O_2$	[154]
$LaNiO_3$	Ofloxacin [10 ppm]	0.2 g L^{-1}	0.5 g L^{-1}	93% at 10 min	50% at 1 h	$^1O_2$	[155]
$LaMnO_3$	Ofloxacin [10 ppm]	0.2 g L^{-1}	0.5 g L^{-1}	90% at 30 min	–		
$LaFeO_3$	Ofloxacin [10 ppm]	0.2 g L^{-1}	0.5 g L^{-1}	15% at 30 min	–		
$LaCoO_3$/ZrO_2	RhB [10 ppm]	0.1 g L^{-1}	0.1 g L^{-1}	100% at 1 h	–	$SO_4^{\cdot-}$	[157]
$CoTiO_3$ nanofiber	Amaranth [50 ppm]	0.1 g L^{-1}	0.1 g L^{-1}	≈100% at 0.5 h	–	$SO_4^{\cdot-}$, $\cdot OH$	[159]

Cobalt as one of the TM elements with notable activity in both homogeneous and heterogeneous activation of persulfate attracts tremendous attention.[146] Thus numerous cobalt-based perovskite oxides catalysts have been prepared for sulfate radical-based AOPs. However, the toxicity induced by cobalt ions leaching retarded the Co-based catalysts application. To tackle Co^{2+} leaching problem, stabilizing cobalt in perovskite lattice by doping demonstrates an effective strategy. Previous studies revealed that more stable cubic perovskite $SrCoO_{3-\delta}$ can be efficiently stabilized by a low concentration B-site element substitution and show enhanced electrical conductivity and oxygen permission activities.[66,147] Miao synthesized Ti-doped $SrCoO_{3-\delta}$ with a cubic structure for activating PMS.[42] It was found that a trade-off between catalytic activity and Co^{2+} leaching level exists in the PMS/$SrCo_{1-x}Ti_xO_{3-\delta}$ system. Thus an optimized composition of $SrCo_{0.6}Ti_{0.4}O_{3-\delta}$ with minimized cobalt leaching, moderate activity, and good stability was used for phenol removal, giving a performance of 77% TOC removal and a 3.1 mg L^{-1} Co leaching at pH 3–5 within 5 h. Besides, the basic and natural reaction system favors the catalytic process and minimizes the Co leaching. This synergetic effect among B-site host and doped element was also found in magnetic double perovskite Sr_2CoFeO_6 nanoparticles, which were prepared by sol-gel method and firstly employed for the PMS activation.[148] The

double perovskite oxide exhibited superior catalytic capacity for bisphenol elimination (via PMS activation) with a lower activation energy of 14.085 kJ mol^{-1} to the $SrFeO_3$ and $SrCoO_3$ catalysts at neutral pH. This illustrates that the synergetic effect indeed exists to promote the ROS evolution due to the accelerated reduction of Fe in B-site. Another identical theory was concluded by Lu et al. utilizing doping method with Cu to tailor the catalytic activity of $LaCo_xM_{1-x}O_3$ towards PMS decomposition and ROS generation.[32] A bimetallic system with Co^{2+}/Co^{3+} and Cu^{1+}/Cu^{2+} redox repairs was formed while Cu ions were incorporated into the lattice. With the presence of Cu^{1+}/Cu^{2+} (0.17 V, versus SHE), the Co^{2+}/Co^{3+} (1.81 V, versus SHE) redox cycle was accelerated because of the reduction of Co^{3+} to Co^{2+} can be facilitated by Cu^{1+}. The detailed mechanism is shown in the following equations (Equations (20–26)). The divalent Co and monovalent Cu act as active sites to react with surface absorbed PMS to produce reactive species. Subsequently, Co^{3+} and Cu^{2+} would accept electrons from PMS to fulfill the redox cycles and maintained the active sites.

$$Co^{2+} + HSO_5^- \rightarrow Co^{3+} + SO_4^{\cdot-} + OH^- \tag{20}$$

$$Cu^{1+} + HSO_5^- \rightarrow Cu^{2+} + SO_4^{\cdot-} + OH^- \tag{21}$$

**ADVANCED
SCIENCE NEWS**

www.advancedsciencenews.com

**ADVANCED
FUNCTIONAL
MATERIALS**

www.afm-journal.de

$$SO_4^{-} + OH^{-} \rightarrow SO_4^{2-} + {}^{\cdot}OH \tag{22}$$

$$Co^{3+} + HSO_5^{-} \rightarrow Co^{2+} + SO_5^{\cdot-} + H^{+} \tag{23}$$

$$Cu^{2+} + HSO_5^{-} \rightarrow Cu^{1+} + SO_5^{\cdot-} + H^{+} \tag{24}$$

$$SO_5^{\cdot-} + O^{2-} \rightarrow SO_4^{\cdot-} + H_2O \tag{25}$$

$$Co^{3+} + Cu^{1+} \rightarrow Co^{2+} + Cu^{2+} \quad (E^0 = 1.64\ V) \tag{26}$$
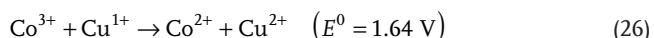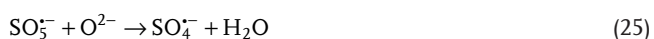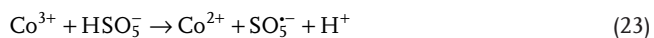
In order to have a further understanding of B-site element doping effects on the activity and stability, Shao and co-workers prepared a series of Mn-doped $LaCo_{1-x}Mn_xO_{3+\delta}$ (x = 0, 0.3, 0.5, 0.7, and 1.0) oxides with over stoichiometric oxygen and investigated their respective performances.[65] Interestingly, enhanced activity and stability appeared to well correlate with the electron filling (e_g) of Co in B-sites. Thus, a volcano-shaped correlation was observed (Figure 3c), in which $LaCoO_{3-\delta}$ and $LaCo_{0.5}Mn_{0.5}O_{3+\delta}$ exhibited superior catalytic with e_g occupancy of 1 and 1.22, respectively. It indicates that the electron structure of B-site element governs the activity and stability of catalyst essentially towards PMS activation. Moreover, the improved stability of $LaCo_{0.5}Mn_{0.5}O_{3+\delta}$ among various catalysts is related to its stronger relative acidity, endowing $LaCo_{0.5}Mn_{0.5}O_{3+\delta}$ strong residence against the metal leaching. For better understanding of the intrinsic mechanism and structure-activity relationship, theoretical investigation via computational chemistry is required.

A-Site Inert Element Tailoring: Alkaline or alkaline rare-earth metal elements in A-site are always inert towards PMS activation. Nevertheless, indirect effects induced by A-site cations have essential contribution to the catalytic performance, since an accuracy control of phase structure and B-site TMs valence can be achieved by means of A-site element adjustment. Additionally, some physical properties, like surface chemistry and texture can also be altered via A-site element tailoring.

Recently, systematic research has been conducted to examine the influence of different A-site rare-earth metals on heterogeneous catalytic degradation of phenol.[149] A series of cobalt-containing perovskite oxides of $ACoO_3$ (A = La, Ba, Sr, and Ce) were employed to activate PMS for phenol degradation. A comparable activity can be attained for the samples of La and Sr in A-site, in which a 68% and 65% TOC removal in 6 h were obtained. The overall performance for all these samples follow the order of $SrCoO_3 > LaCoO_3 > BaCoO_3 > CeCoO_3$. This study reveals that the performance difference among these samples could be ascribed to the crystallinity instead of the slight change of specific surface area and pore volume, which means lower crystallinity induced by A-site elements has adverse impact on the activity.

Sr-doped $La_{0.4}Sr_{0.6}MnO_{3-\delta}$ was used for the PMS activation and organics degradation.[150] Notably, it was confirmed that A-site doping strategy can boost the catalytic behavior for PMS activation, which showed about 6 and 41 times higher than $LaMnO_3$ and the cobalt spinel oxide, respectively. Mechanism study reveals that the optimized surface properties were the main contribution of A-site foreign inert element doping.

A large amount of positively charged oxygen defects were created on the surface, which favored the adsorption and decomposition of PMS. As a result, the lower activation energy would be achieved on $La_{0.4}Sr_{0.6}MnO_{3-\delta}$ (44.3 kJ mol^{-1}) than $LaMnO_3$ (67.8 kJ mol^{-1}).
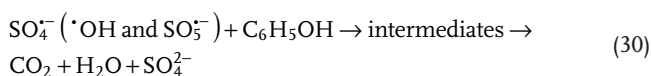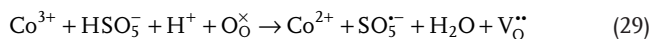
In addition, despite the inertness of A-site doped element, it can affect the electronic structure and coordination environment of the B-site TM elements, which then introduce effects on the catalytic behavior. Duan et al. prepared $Ba_{0.5}Sr_{0.5}Co_{0.8}Fe_{0.2}O_{3-\delta}$ (BSCF) for PMS activation and they found that BSCF perovskite oxide was exclusively effective for PMS activation to produce free radicals, which was benefited from the introduction of Ba into A-site.[151] Less electronegative Ba (χ = 0.9) not only enhances the phase stability but also can maintain a high level of oxygen vacancies for BSCF. Of importance, due to the lower electronegativity of Ba comparing with Co (χ = 1.9), high density electrons would surround Co, benefiting the charge transfer and redox cycles. Moreover, the A-site metals can secure cobalt at B-site with a lower valence state for donating electrons to PMS simultaneously for radical generation.

3.3.2. The Role of Oxygen Vacancy and Defects Engineering

Mixed conducting double perovskite oxide $PrBaCo_2O_{5+\delta}$ (PBC) was employed as heterogeneous catalyst for oxidizing MB and phenol by PMS activation.[27] The catalytic activity of this kind of ionic-electronic conducting perovskite is much higher than the benchmark catalyst Co_3O_4 over a wide pH range, where the TOF was increased by 196-fold against Co_3O_4. The enhanced PMS molecules adsorption ability of PBC achieved by the rich oxygen vacancies on the PBC catalyst surface contributed to the cleavage of the O-O bond and thus activating PMS to produce powerful oxidative $SO_4^{\cdot-}$ and $^{\cdot}OH$ radicals, which is an important reason causing performance difference between PBC and Co_3O_4. The activation and degradation pathways were displayed from Equations (27–30) and shown in **Figure 10**a.[27] Moreover, due to the good ionic conductivity and high oxygen vacancy concentration of PBC catalyst, the oxygen ion diffusion near the surface layer would aid the alteration of cobalt valences, which also partially promoted the catalytic activity. A similar observation has also been made in BSCF/PMS system, in which the immigration of oxygen vacancies in the subsurface or surface layer is partially responsible for the high charge conductivity and replenishing the consumed surface oxygen defects.[151] These studies directly revealed the crucial role of oxygen vacancies in PMS activation. Likewise, the oxygen transfer due to the mobility of oxygen vacancies has been proposed in Cu doped $LaCoO_3$ perovskite.[32] Oxygen vacancies serve as active sites for oxygen adsorption, where the adsorbed oxygen can be transformed to the lattice oxygen which could be further released to form active singlet oxygen. Besides, oxygen vacancies may bind with water to form surface hydroxyl functional groups that enable the electron transfer from Co^{2+}/Co^{3+} to PMS for O—O fracture.[151] Similar results have also been reported by other researcehrs that the surface hydroxyl groups would facilitate the chemical bonding with PMS via TM-O-H-O-SO₃ and prompt the electron transfer from reduced TM to PMS molecules via inner-sphere interaction.[27]
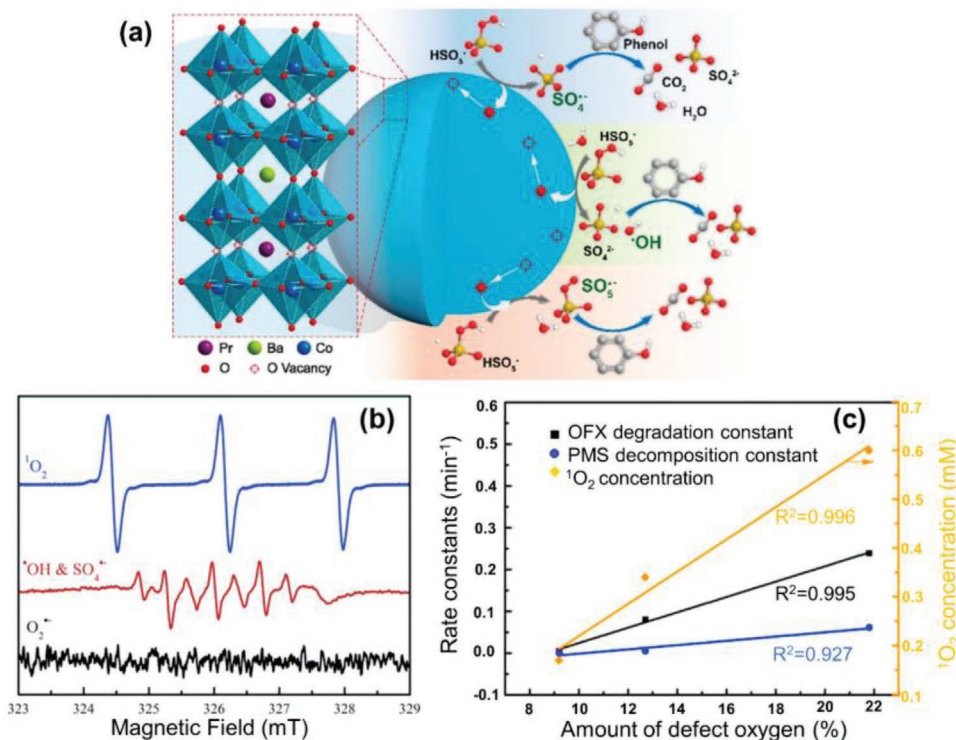
Figure 10. a) Schematic illustration of PMS activation and phenol oxidation process over $PrBaCo_2O_{5+\delta}$. Reproduced with permission.[27] Copyright 2017, American Chemical Society. b) EPR spectra of ROS. c) Correlations among oxygen defect degree and ofloxacin oxidation kinetics, PMS decomposition constant, and $^1O_2$ concentration. Reproduced with permission.[155] Copyright 2018, Elsevier.

$$Co^{2+} + HSO_5^- + V_O^{\bullet\bullet} \rightarrow Co^{3+} + SO_4^{\bullet-} + H^+ + O_O^\times \qquad (27)$$

$$Co^{2+} + HSO_5^- + H_2O + V_O^{\bullet\bullet} \rightarrow Co^{3+} + SO_4^{\bullet-} + {}^\bullet OH + 2H^+ + O_O^\times \quad (28)$$

$$Co^{3+} + HSO_5^- + H^+ + O_O^\times \rightarrow Co^{2+} + SO_5^{\bullet-} + H_2O + V_O^{\bullet\bullet} \qquad (29)$$

$$SO_4^{\bullet-} ({}^\bullet OH \text{ and } SO_5^{\bullet-}) + C_6H_5OH \rightarrow \text{intermediates} \rightarrow CO_2 + H_2O + SO_4^{2-} \qquad (30)$$
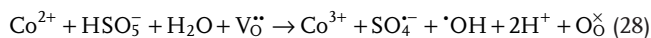
Where $V_O^{\bullet\bullet}$ and $O_O^\times$ represent double-charged oxygen vacancy and oxygen ion in lattice.

Very recently, Rao et al. observed that the chemical bonding formation between Fe^{3+} (B-site) and PMS molecule was favored in the presence of surface oxygen vacancies in the perovskite oxide surface.[152] Additionally, non-radical process was found in the perovskite oxide/PMS reaction system. singlet oxygen ($^1O_2$) was first identified as the main ROS in perovskite/PMS system.[153] Surface oxygen vacancies were involved in the oxidation process.[154] In addition to sulfate and hydroxyl radicals as mentioned above, non-radical process, like singlet oxygen can also be generated with the aid of surface oxygen deficiency. The related non-radical processes are shown in the following equations (Equation (31,32)), where oxygen vacancy ($V_O^{\bullet\bullet}$) evolved to active oxygen species ($O_O^\times$) which react with PMS for $^1O_2$ generation. This theory was further evidenced by another study using $LaMO_3$ (M = Fe, Zn, Mn, Ni) for PMS activation, where $^1O_2$ as dominant ROS (Figure 10b) and an oxygen defect

dependent PMS activation mechanism was proposed.[155] It was found that the oxygen defects of M = Fe, Mn, and Ni materials were 9.2, 12.7, and 21.8%, respectively, which is in good accordance with the organic degradation efficiency, PMS decomposition rate, and $^1O_2$ concentration showed in Figure 10c.

Coincidentally, another study by Shao and Co-workers again manifested $^1O_2$ as dominant ROS due to the existence of surface oxygen defects generated by introducing inert Sr to oxygen excess $LaMnO_{3+\delta}$.[150]

$$V_O^{\bullet\bullet} \rightarrow O_O^\times \qquad (31)$$

$$O_O^\times + HSO_5^- \rightarrow HSO_4^- + {}^1O_2 \qquad (32)$$

Numerous studies proved the vital roles of oxygen vacancies in the reaction of PMS activation and organic pollutant decomposition. Besides to A/B-site doping strategy, a new protocol via cation defect engineering, was proposed by creating abundant oxygen defects.[156] Improved oxygen vacancy concentration of Ag exsolved $La_{0.8}Ca_{0.2}Fe_{0.94}O_{3-\delta}$ with B-site cation deficiency rendered this catalyst enhanced performance for activating PMS to generated highly oxidative sulfate radicals.

3.3.3. Surfacing Engineering and Morphology Control

Various approaches have been employed for the perovskite-based materials preparation to optimize surface chemistry and

ADVANCED
SCIENCE NEWS
www.advancedsciencenews.com

ADVANCED
FUNCTIONAL
MATERIALS
www.afm-journal.de

alleviate the adverse influence endowed by low surface area and pore volume for PMS activation. To this end, zirconia supported $LaCoO_3$ and aluminum oxide supported $LaCoO_3$ nanostructure were synthesized and employed as heterogeneous catalyst for organic pollutant elimination.[157,158] Compared to the bulk $LaCoO_3$ powder, the nanostructured materials exhibited enlarged surface area (≈10 times than bulk $LaCoO_3$) and enhanced catalytic activity for activating PMS. $CoTiO_3$ nanofiber fabricated using the electrospun technique has also been reported.[159] The nanoscale fibrous structure with mesoporous structure enables the material a relatively enlarged surface area and porosity. As a result, PMS activation and amaranth dye oxidation efficiency were further improved in comparison to the bulk materials. Besides, the perovskite-based hollow fiber membrane was fabricated and assembled as membrane reactor for AOP, which exhibited merits of easy operation, high regeneration efficiency, and low energy requirement.[160]

Surface chemistry is of significance in terms of PMS activation and organic oxidation since these two processes proceed over the catalyst surface either in active B-site cations or defects.[152] In addition, metal leaching induced by erosion occurs on the catalyst surface. Thus, rational surface tailoring such as surface functionalization and constructing heterojunction would enhance the catalytic activity and suppress the metal leaching to some extent. A facile hydrothermal post-treatment was applied to enhance the surface properties of $SrCo_{0.6}Ti_{0.4}O_{3-\delta}$ (SCT) for ROS evolution.[154] One layer CoOOH with thin 2D nano-sheet morphology was in situ grown over the SCT surface via the hydrothermal process, as shown in **Figure 11**. The catalysts experienced post-treatment exhibited significant improvement for phenol removal (100% removal in ≈20 min), while pristine SCT showed inferior activity, where complete

Figure 11. Morphologies of a) pristine $SrCo_{0.6}Ti_{0.4}O_{3-\delta}$ (SCT) and b–f) SCT@CoOOH hybrids by hydrothermal treatment at varied conditions (120, 150, and 180 °C for 12, 6, and 24 h). Reproduced with permission.[154] Copyright 2018, American Chemical Society.

degradation was achieved in 35 min. This enhancement was ascribed to the optimized surface properties, including increased surface area (22.1 m^2g^{-1}), positively charged surface (3.5 mV), improved electron transfer ability, high content of surface oxygen defects, and the synergistic effects between SCT and CoOOH. More importantly, cobalt leaching could be suppressed by the facile hydrothermal method and thus the stability of catalysts was further improved. Besides the proposed surface modification method via post-treatment, other well-developed techniques such as highly durable surface coating and facet engineering to expose more stable and active facets might be promising strategies to overcome the trade-off relationship between the activity and metal leaching.
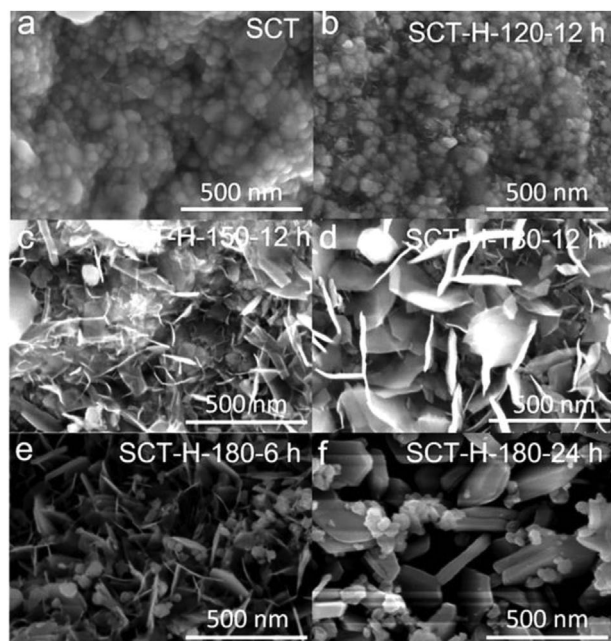
3.4. Perovskite Oxides in Catalytic Ozonation

The main advantage of catalytic ozonation is the ability to enhance the mineralization capacity of organic components via ROS generated from ozone activation. A series of perovskite oxides with various compositions have been tested for the catalytic ozonation process. Most of the researchers found that the surface properties play more important roles for the ozone activation and organics degradation, like oxygen vacancies arrangement, surface charge state, surface Lewis acid sites, and functional groups. In this subsection, we will focus on the catalytic ozonation process and strategies for performance enhancement using these perovskite oxide catalysts.

3.4.1. Significance of Surface Properties

In 2006, Carbajo et al. evaluated the catalytic ozonation performance of B-site doped $LaTi_{1-x}M_xO_3$ (M = Cu and Co) perovskite with varied doping content.[161] It was found that $LaTi_{0.15}Cu_{0.85}O_3$ possessed notable activity for organics mineralization. Afterward, several works have been conducted by their group based on $LaTi_{0.85}Cu_{0.15}O_3$ to evaluate the effects of main operating parameters (temperature, ozone dosage, initial organics concentration, and pH) and illustrate the reaction mechanisms via kinetics.[162,163] For instance, Rivas et al. suggested a dual adsorption Langmuir-Hinselwood mechanism for $LaTi_{0.15}Cu_{0.85}O_3$ catalytic ozonation of pyruvic as only surface reaction was observed to govern the whole process.[162]

Meanwhile, several studies attempted to pursue the detailed surface reaction mechanism. In comparison with direct ozonation process, the amount of ozone consumed in the organic depletion showed no much difference for the catalytic ozonation processes, but a significant organic mineralization enhancement greater than 90% was achieved in the presence of perovskite catalysts versus the 35% for direct ozonation.[164] This provides evidence that the catalysts can promote the free radical generation and these radicals with higher oxidation potential than ozone account for the improved mineralization. A similar phenomenon was demonstrated by Beltrán et al. that both direct and indirect ozonation had similar initial pollutant decomposition efficiency, but the indirect process catalyzed by perovskite exhibited significantly higher capability in further degradation of ozone-recalcitrant intermediates.[165,166] They
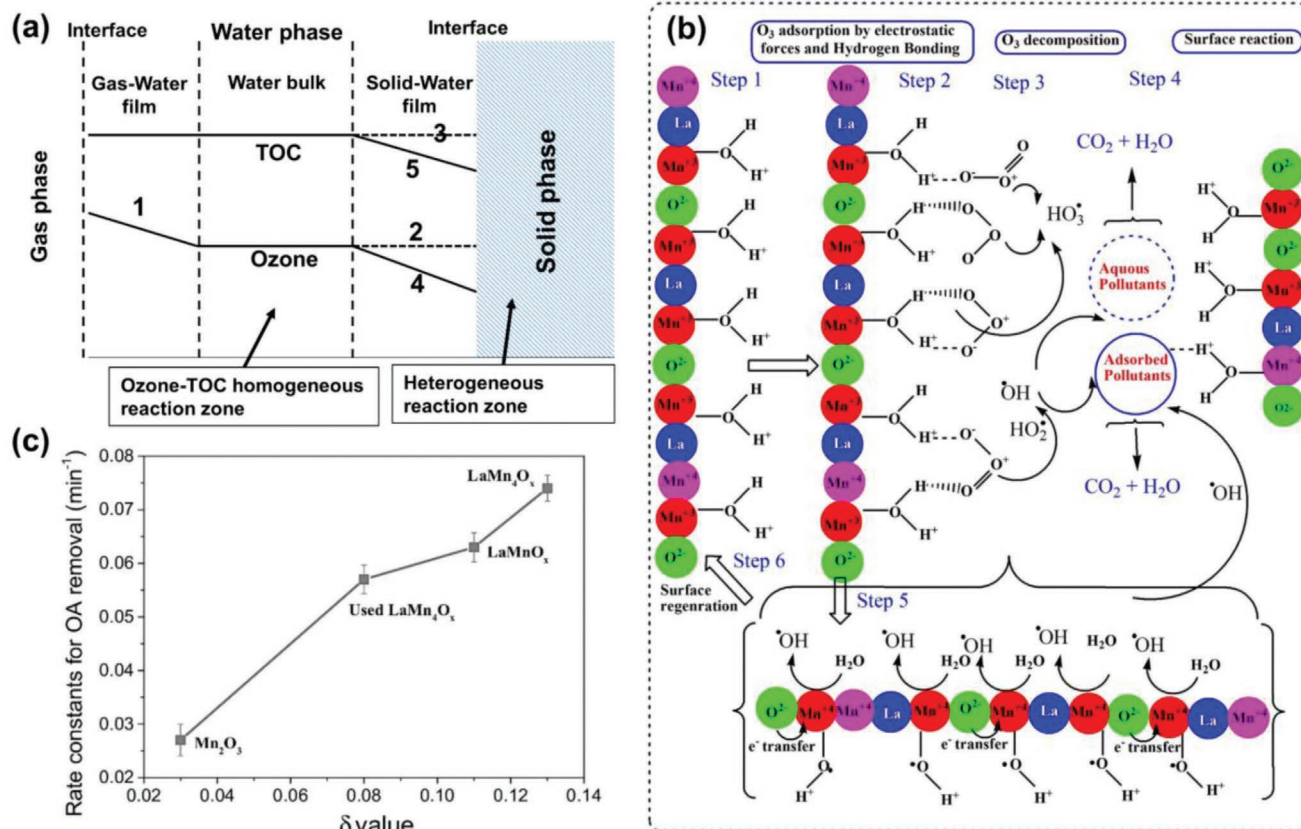
Figure 12. a) A diagram of film theory in catalytic ozonation process; 1: ozone depletion process due to the mass transfer residence at gas–liquid interface; 2 and 3: uniform ozone and TOC profiles, respectively, as the control of surface reaction; 4 and 5: non-uniform profile of ozone and TOC, respectively, because of the occurrence of catalytic ozonation process. Reproduced with permission.[165] Copyright 2009, Elsevier. b) Mechanism illustration of catalytic ozonation process over LaMnO₃. Reproduced with permission.[169] Copyright 2017, Elsevier. c) Correlation between the oxalic acid degradation constant and oxygen vacancy content. Reproduced with permission.[43] Copyright 2019, Elsevier.

believed that two stages exist in the catalytic ozonation process, that is, decomposition of organic substance by direct ozonation in water bulk and subsequent mineralization of refractory intermediates at catalyst surface by radicals. Thus a film theory was proposed for the heterogeneous catalytic ozonation as shown in **Figure 12**a, where the second stage at solid–water interface is more determined by mass transfer kinetics (external ozone diffusion to the liquid-solid interface).

Later, Orge et al. suggested a more plausible mechanism for perovskite oxide-based catalytic ozonation, which not only comprises surface reaction but also involves the liquid bulk reaction supported by ·OH.[167] For the ·OH evolution, it is believed that superoxide species generated by activating adsorbed ozone favored the intermediate (H_2O_2) production to evolve ·OH or react with ozone to yield ·OH.[168] A further understanding of the influence of catalyst surface properties on ozone adsorption was attempted by Afzal et al.[169] Surface charge is the most important factor and can be adjusted by pH value change. In case of LaMnO₃, the highest activity was achieved at a neutrally charged surface (Mn-OH) attained at pH 8.98, while a slightly descending performance was revealed for protonated surface (Mn-OH₂⁺) at pH 3 and deprotonated surface (Mn-O⁻) at pH 11. Given the electrophilic and nucleophilic nature of ozone, the protonated surface (−OH₂⁺) possessed weaker nucleophilic

ability to the O of neutrally charged surface (−OH) but the deprotonated surface cannot provide electrophilic H to ozone molecules. Therefore, the O₃ adsorption and binding abilities of both positive and negative charged surface were alleviated, which led to a negative effect on O₃ activation and ·OH evolution. In addition to the ozone adsorption, the significant influence of surface charge state on organic molecules adsorption was also justified. Low pH value leads to the positively charged surface and facilitates the electrostatic adsorption of organics, which contributes to the TOC removal. However, the decreased mineralization caused by deprotonated surface with weak adsorption has been demonstrated.[169] The schematic of ozone adsorption, activation, and organic pollutant decomposition process has been presented in Figure 12b.

Although the aforementioned researches have clearly clarified the surface dominant reaction mechanism and evaluated the influence factors on adsorption, fewer studies give insights into the detailed O₃ decomposition behavior and its effect on subsequent ROS generation. A theoretical study through density functional theory (DFT) calculation gives an explicit demonstration of the adsorption process and O₃ disassociation pathways.[43] Results show that Lewis acid sites, like surface hydroxyl groups, oxygen vacancies, and B-site cations (i.e., Mn) would be active to facilitate the adsorption. For the

**ADVANCED
SCIENCE NEWS**
www.advancedsciencenews.com

**ADVANCED
FUNCTIONAL
MATERIALS**
www.afm-journal.de

hydroxyl groups on the surface, simulation indicates that the single-bonded O atom in ozone molecule can bond with surface hydroxyl groups via weak covalent bond, and the length of O—O bond in O_3 can be stretched slightly due to the lower adsorption energy (–0.46 to –0.79 eV for different configurations of hydroxyl groups). This suggests the surface hydroxyl groups may be active for the ozone decomposition. Moreover, a stronger bond between single-bond O in ozone and B-site Mn was found with higher adsorption energy (–1.48 eV), the length of O—O bond of O_3 increased from 1.285 to 1.524 Å, which was proved to be more efficient for O_3 activation. The highest active oxygen vacancies are illustrated in Section 3.4.2. In summary, the ozone could be decomposed into adsorbed atomic oxygen (O_{ad}^*) and free peroxide ($^*O_2$) on the active sites (oxygen vacancies, B-site cations, and surface hydroxyl groups) by the means of stretching the O—O bond. Then the decomposed oxygen active species initiated the following radical and non-radical process, shown in Equations (33–37).

$$O_3 \xrightarrow{\text{Active seites}} O_2^* + O_{ad}^* \tag{33}$$

$$O_{ad}^* \xrightarrow{\text{Pronated}} {}^\bullet OH \tag{34}$$

$$O_2^* \rightarrow HO_2^{\bullet-} + O_2^{\bullet-} \tag{35}$$

$$O_{2\,free}^* \xrightarrow{\text{Pronated}} HO_{2\,free}^\bullet \xrightarrow{O_3} {}^\bullet HO_{free} \tag{36}$$

$$O_2^* \rightarrow {}^1O_2 \tag{37}$$

Another finding by Zhang et al. also verified the importance of surface functional groups and oxygen species by applying $LaFeO_3$ in bromate elimination and organics oxidation.[170] The superior bromate elimination behavior of $LaFeO_3$ was attributed to the surface hydroxyl groups which interacted with intermediate H_2O_2 to form $[Fe-H_2O_2]_s$ complex for efficient bromate reduction. But its low efficiency in organics mineralization was caused by the lack of sufficient surface oxygen species (low ratio of $O^{2-}/$-OH), thus leading to a weak ozone decomposition and ${}^\bullet$OH evolution. This observation is in accordance with the former studies.[167]

3.4.2. The Role of Oxygen Vacancy and Defects Engineering

Oxygen vacancies were considered as the adsorption sites for the oxygen firstly in the perovskite/ozone system by Orge.[167] Very recently, Wang et al. systematically investigated the defect roles in the perovskite oxide-based catalytic ozonation process through the experiment and theoretical calculation.[43] A positive correlation between the content of oxygen vacancy and the reaction rate constant for oxalic acid destruction was revealed in Figure 12c. By decreasing the ratio of La/Mn for perovskite, oxygen nonstoichiometry increase thus induced improved removal efficiency. This evidenced the favorable effects of oxygen vacancies on catalytic ozonation. DFT calculations gave further insight to clarify the detailed functions of oxygen defects on O_3 stimulation. It was found that oxygen vacancies acted not

only as ozone adsorption sites but also as essential active sites for O_3 direct dissociation. The O—O bond of adsorbed ozone molecule on oxygen vacancy could be broken spontaneously due to the strong Lewis acidity of oxygen defects. And calculation results show that the adsorption energy between ozone and oxygen defects was –2.04 eV that was even higher than the adsorption among ozone and Mn sites (–1.48 eV). Such strong adsorption energy and O_3 dissociation ability indicated that oxygen vacancies could serve as more powerful active sites, which would favor the ROS formation and thus contribute to the mineralization.

3.4.3. Bulk Composition Tailoring

The effects of A-site cation tailoring on catalytic ozonation have been investigated.[167] The indirect effects may be caused by the differences in phase structure, cation size, and electronic activities. For example, the catalytic ozonation activities of the Ce doped $La_{0.8}Ce_{0.2}Al_{0.7}Cu_{0.3}O_3$ exhibited remarkable improvement in oxalic elimination compared to its parent $LaAl_{0.7}Cu_{0.3}O_3$, which can be explained by the formation of amorphous phases due to Ce doping.

Similarly, B-site dopants also significantly affect the catalytic ozonation efficiency. As mentioned above, B-site cations with variable oxidation states can be tuned to fulfill the redox cycles required in the catalytic process. Lanthanum-based perovskite $LaMO_3$ (M = Fe, Ni, Co, and Mn) has been probed for its effects in the ozonation process and a descending trend of catalytic ozonation activities was obtained as $LaMnO_3$ > $LaCoO_3$ > $LaNiO_3$ > $LaFeO_3$ (**Table 4**).[167] However, considering both the stability and catalytic performance, $LaCoO_3$ was regarded as a better catalyst with good stability though $LaMnO_3$ exhibited slightly higher activity. This confirms the sensitivity of catalytic ozonation activity with the varied B-site cations. A more recent study concludes that the superior performance of $LaCoO_3$ versus $LaFeO_3$ is stemmed from its higher hydroxyl radical production capability, which accounts for the high efficient TOC removal.[170]

3.4.4. Surfacing Engineering and Morphology Control

Besides the bulk composition tailoring, external influence should be considered alternatively to enhance the catalytic ozonation activity, such as engineering methods to increase surface area and/or pore volume of perovskite oxides. For example, nano-casting technique using SBA-15 zeolite as the template was applied to prepare perovskite oxides (NC-$LaMnO_3$ and NC-$LaFeO_3$) with surface area up to 100 m^2 g^{-1}, which significantly boosted the removal efficiency of 2-chlorophenol.[169] In order to improve electron transfer, constructing composite, like coupling g-C_3N_4 with $LaCoO_3$ perovskite oxide (CN/LCO) appeared to be a very efficient way to enhance catalytic ozonation.[171] A facile compositing approach by sintering $LaCoO_3$ with urea could yield the ideal composite with chemical interaction between layer-structure g-C_3N_4 and $LaCoO_3$. The conjunction of cobalt and aromatic π ring via interface Co—O—C bond could promote electron transfer, thus accelerating the Co^{2+}/Co^{3+} redox cycles

ADVANCED
SCIENCE NEWS
www.advancedsciencenews.com

ADVANCED
FUNCTIONAL
MATERIALS
www.afm-journal.de

Table 4. Catalytic activity of selected perovskite oxide catalysts for catalytic ozonation process.

Materials	Organic pollutants	Catalyst loading	O_3 dosage	Degradation rate	TOC removal	Main radicals	Ref.
$LaMn_4O_x$	Oxalic acid [50 ppm]	0.2 g L^{-1}	20 ppm	100% at 45 min	–	$^\bullet OH$, $^1O_2$, $O_2^{\bullet-}$	[43]
$LaTi_{0.15}Cu_{0.85}O_3$	Pyruvic acid [5 m$_M$]	1 g L^{-1}	50 ppm	100% at 150 min	60% at 6 h	–	[162]
$LaTi_{0.15}Cu_{0.85}O_3$	Gallic acid [1 m$_M$]	2.5 g L^{-1}	5 ppm	100% at 60 min	>90% at 3 h	–	[164]
$LaCoO_3$	Reactive Blue 5 [50 ppm]	0.1 g L^{-1}	50 ppm	100% at 15 min	100% at 3 h	$^\bullet OH$	[167]
$LaMnO_3$	Oxalic acid [1 m$_M$]	0.1 g L^{-1}	50 ppm	100% at 60 min	100% at 2 h	$^\bullet OH$	[167]
$NC\text{-}LaMnO_3$	2-CP [50 ppm]	0.3 g L^{-1}	20 ppm	100% at 45 min	80% at 75 min	$^\bullet OH$	[169]
$LaCoO_3$	Benzotriazole [10 ppm]	0.5 g L^{-1}	2 ppm	100% at 15 min	65% at 2 h	$^\bullet OH$	[170]
$LaFeO_3$	Benzotriazole [10 ppm]	0.5 g L^{-1}	2 ppm	100% at 20 min	65% at 2 h	$^\bullet OH$	[170]
$g\text{-}C_3N_4/LaCoO_3$	Benzotriazole [10 ppm]	0.25 g L^{-1}	1 ppm	–	≈60% at 2 h	$^\bullet OH$, $^1O_2$, $O_2^{\bullet-}$	[171]
	Bromate [0.1 ppm]	0.25 g L^{-1}	1 ppm	66.6% at 90 min	–	H_2O_2	

for ozone activation. Moreover, the existing nitrogen-vacancy in the composite provided additional active sites for O_3 activation and $^\bullet OH$ yielding. All these features of the composite are conducive for ROS and H_2O_2 generation thus improving the organic contaminant mineralization and bromate elimination. Efforts have also been devoted to controlling the morphology to expose more active sites. For example, a hierarchical $LaMnO_{3-\delta}$ sphere with minor α-Mn_2O_3 phase was prepared and exhibited higher catalytic activities than the agglomerated structure for catalytic ozonation.[43]

3.5. Perovskite Oxides in O_2 Dark Activation Process

Dye wastewater discharge from textile industries has caused serious environmental contamination. Among the textile dyes discharged (28 000 tons per year), azo dyes are the most common class and account over 50%.[91,172] As a result, dyes-containing wastewater has become an important issue and various remediation technologies have been developed. Nevertheless, popular AOPs, such as photodegradation shows undesirable degradation efficiency due to the low transparency of these dye solutions at high concentration.[173] Besides, Fenton/Fenton-like process, sulfate-based radical system, and catalytic ozonation process are unsuitable for industrial applications since large amounts of peroxides as the oxidants are required, increasing material cost. Therefore, attempts have been made to achieve efficient dye degradation without the aids of external stimulates (i.e., light illumination and/or additional peroxides). In this regard, some researchers have studied O_2 activation via perovskite oxide-based catalysts to generate ROS for water remediation under dark ambient conditions.

3.5.1. ABO_3 Perovskite Oxides-Based Catalysts

Effects of Surface Properties: As aforementioned, extensive works have been performed to study the applications of ABO_3 perovskites in AOPs, especially for sulfate radicals generation, Fenton-like system and catalytic ozonation.[170,174,175] Some efforts have also been devoted to the O_2 activation by ABO_3 perovskites under ambient atmosphere without light. For

example, a series of $LaCoO_{3-\delta}$ perovskites with different sintering temperatures had been synthesized via sol-gel method and evaluated for the dye degradation under dark conditions but with low efficiency.[176] Based on the phenomenon observations, the surface characters of catalysts play important roles in dyes degradation, where the oxygen vacancy density, valence of B-site cations, and perovskite structure are sensitive to the catalytic degradation process. By B-site element adjustment, $LaNiO_{3-\delta}$ showed a higher degradation rate (94.3% removal in 4 h) against $LaCoO_{3-\delta}$ under dark conditions, which exhibited an opposite trend for PMS activation by $LaCoO_3$ perovskite oxide for dyes degradation.[146,177] Because of the flexibility of perovskite composition in both A- and B-sites, other ABO_3 perovskite oxides have been designed and applied in dyes degradation. Leiw et al. prepared $SrFeO_{3-\delta}$ for Acid Orange 8 (AO8) and BPA elimination at dark ambient and explored the insight mechanism.[178] Faster degradation of AO8 than BPA can be attributed to the strong adsorption of anionic AO8 and positively charged surface of catalyst. In addition, superoxide radicals ($O_2^{\bullet-}$) were identified as ROS in this system and their generation might be related to oxygen vacancies. Previous studies also indicated that surface oxygen vacancies favor the adsorption and decomposition of O_2, which provides the channel for electrons transfer and thus contributes to O_2 activation.[179,180] Another mechanism was proposed by Sun et al. that oxygen vacancies promote the formation of adsorbed oxygen species, such as O_2^{2-} and O^-, which exhibit strong electrophilic properties and can attack the pollutant molecules in the electron-rich region.[181] Although researchers argue the degradation mechanism, the significant roles of oxygen vacancies and other surface features are clear.

Bulk Composition Tailoring: Introduction of minor content of Ce, Ba, Ca, and Mg at A-site of ABO_3 was reported to improve the catalytic activity for organics degradation under dark conditions without adding extra oxidants.[88,182] For instance, $Sr_{0.85}Ce_{0.15}FeO_{3-\delta}$ perovskite oxide was developed and evaluated to degrade the Orang II (OII) and RhB without light assistance.[88] Partial substitution of divalent Sr by tetravalent Ce in A-site can stabilize the perovskite structure and form cubic phase, which benefits both ionic and electrical conductivity.[66,183,184] Besides, due to the extra positive charge of A-site, the redox couple of Fe^{3+}/Fe^{4+} was maintained, which can improve the catalytic activity.[183] More importantly, doping

at A-site induced surface property change, where more surface oxygen defects were formed.[185] This enhanced the interaction between the catalysts and O_2 as oxygen defects served as active sites for oxygen activation. Besides Ce, other elements like Ba, Ca, and Mg have been incorporated into $SrCoO_3$ for dyes elimination.[182] It was found that better stability was achieved for doped samples in the cycle use than the pristine $SrCoO_3$ which was easily decayed. The Ca-doped perovskite showed the best catalytic performance and stability among all prepared catalysts, probably due to the synergistic effects of Sr and Ca in A-site to enhance the performance. However, to our knowledge, no reports have been published to clarify such effects for AOPs. Chen et al. partially substituted Sr with Ca in A-site and investigated the effects of Ca-doping on azo dye dark degradation.[91] Higher Ca-doping can notably enhance the activity in cycle-use, which is ascribed to the basic environment and B-site cations stability maintained by A-site Ca^{2+}. In addition, interaction between dyes and catalysts is the prerequisite step to trigger the catalytic degradation process as electron donation would occur from dyes to catalysts. This also highlights the importance of catalyst surface properties.

In addition to A-site doping, B-site element adjustment/doping is believed to be a more efficient approach to boost the catalytic activity.[186,187] For instance, Cu was used as a B-site dopant to modify $CaSrNiO_3$ perovskite to improve the activation ability of O_2 for azo dyes dark degradation without peroxides and light.[188] It was observed that catalyst containing equal molar composition of Cu and Ni ($CaSrNi_{0.5}Cu_{0.5}O_3$) exhibited the most active reactivity and stability, where 95% degradation and 54% mineralization within 2 h were reached without assistance of light and peroxides. Additionally, Cu-doping also stabilized the Ni in B-site and efficiently reduced the metal. As a consequence, high activity was maintained over 15 cycles during the stability test, which was also ascribed to the conjunctive redox couples of Cu^{1+}/Cu^{2+} and Ni^{2+}/Ni^{3+}.

3.5.2. Layered Perovskite Oxides-Based Catalysts

To date, only limited researches have reported the application of layered perovskite in the area of water remediation (**Table 5**). Platinised D–J type perovskite $Pt-HCa_2Nb_3O_{10}$ and $Pt-WO_3$ were adopted by Dvininov and co-works in 2010 as semiconductors for photocatalytic degradation of MO.[189] Surprisingly, both kinds of semiconductor particles can activate oxygen from air to oxidize MO under dark ambient conditions and without any external excitation (peroxide and thermal input). This was the first study to use a layered D–J perovskite as AOPs catalyst for oxygen activation without external energy input, which differs from the CWAO process demanding high temperature and pressure. A possible mechanism was proposed that the synergistic effects of Brønsted acidity of laminar $HCa_2Nb_3O_{10}$ perovskite with Ca^{2+} in addition with d° center improve the donor ability of lattice oxides, which contributes to the oxygen activation.

In addition to the D–J perovskite, R–P type La_2NiO_4,[190] and $La_4Ni_3O_{10}$[172] perovskite oxides prepared by co-alcoholysis and solution combustion approach, respectively, were employed to degrade 4-chlorophenol (4-CP, anionic organic) and MO (azo dye) without energy input. For 4-CP degradation under dark conditions, La_2NiO_4 exhibited superior catalytic performance with the mineralization of more than 95% in 12 h. In comparison with the light illumination process, the reaction constant (k) and degradation efficiency under dark were much lower, but the calculated activation energy (61 kJ mol^{-1}) was not higher but lower than photocatalysis (73 kJ mol^{-1}), indicating that 4-CP degradation undergoes different reaction pathways in dark degradation process. Further exploration showed that the organics were mainly attacked by hydroxyl radicals ($^{\bullet}OH$) under darkness, the generation of which was associated with the dissolved O_2 from air instead of H_2O as N_2 purging could completely suppress the $^{\bullet}OH$ generation. An electron mediation mechanism was proposed where O_2 is deemed as an electron acceptor and anionic organic 4-CP can donate electrons. The laminar La_2NiO_4 can trap electrons from 4-CP to react with O_2 molecules, which promotes the O_2 activation and $^{\bullet}OH$ production.[190] This might be benefited from the layered structure of La_2NiO_4 to facilitate electron transfer. The critical role of electron transfer was also observed in azo dye (MO) and 4-CP dark degradation over $La_4Ni_3O_{10}$ and La_2NiO_4, respectively. In such a process, the efficiency is quite dependent on the organic categories, perovskite structure, and pH values of the solution or temperatures. Therefore, some layered perovskites display selective reaction with some specific dyes. For example, $La_4Ni_3O_{10}$ can more efficiently decompose cationic dyes, such as RhB and MB, than azo dye MO.[172] This kind of selectivity is related to

Table 5. Catalytic activity of selected perovskite oxide-based activator for oxygen activation without energy input.

Materials	Organic pollutants	Catalyst loading	Degradation rate	TOC removal	Radicals	Ref.
$Sr_{0.85}Ce_{0.15}FeO_{3-\delta}$	OII [10 ppm]	0.75 g L^{-1}	≈65% at 7 h	–	$^{\bullet}OH$	[88]
$Ca_{0.25}Sr_{0.75}CuO_{3-\delta}$	OII [50 ppm]	1 g L^{-1}	≈90% at 1 h	36% at 1 h	$^{\bullet}OH, O_2^{\bullet-}$	[91]
$La_4Ni_3O_{10}$	MO [5 ppm]	–	≈65% at 3.5 h	21% at 8.5 h	$O_2^{\bullet-}$	[172]
$LaNiO_{3-\delta}$	MO [5 ppm]	1.5 g L^{-1}	94.3% at 4 h	–	–	[177]
$SrFeO_3$	BPA [440 μM]	21 mM	–	83% at 24 h	$O_2^{\bullet-}$	[178]
	AO8 [150 μM]	21 mM	100% at 1 h	–	$O_2^{\bullet-}$	
BaSrCoO	OII 20 [ppm]	1 g L^{-1}	78% at 2 h	–	$O_2^{\bullet-}$	[182]
$Ca_{0.5}Sr_{0.5}Ni_{0.5}Cu_{0.5}O_3$	OII 20 [ppm]	1 g L^{-1}	70% at 20 min	≈54% at 2 h	$^{\bullet}OH, O_2^{\bullet-}$	[188]
La_2NiO_4	4-CP [5 μM]	1.5 g L^{-1}	–	95% at 12 h	$^{\bullet}OH, O_2^{\bullet-}$	[190]

**ADVANCED
SCIENCE NEWS**
www.advancedsciencenews.com

**ADVANCED
FUNCTIONAL
MATERIALS**
www.afm-journal.de

the perovskite surface and electron transfer properties. At pH value of 6.1, the positively charged surface of catalysts might favor the electrostatic adsorption of ionized anionic dyes and then promote the electron transfer for O_2 activation.

For a brief summary, layered perovskite oxides possess the great potential to activate the O_2 without external stimulation for organics removal. During the process, laminar perovskite oxides catalysts act as a bridge between the pollutants and O_2 to provide channels for electron fast transfer.[172] However, how the electrons migrate through layered perovskites and how the catalyst promotes the electrostatic interaction with organics still remain unknown deserving further investigation.

3.5.3. Mechanism Elucidation of O_2 Dark Activation for Dyes Degradation

From the perspective of catalysts properties, as aforementioned, among various studies of dyes dark degradation by oxygen activation process, perovskite surface properties such as oxygen defects[176,177] and surface charge state[178] play the key roles for both O_2 activation and dyes decomposition process since electron transfer proceeded over these processes. Therefore, the interaction between catalysts, dissolved O_2 molecules, and dyes are indispensable to trigger the process.

In general, for organics decomposition by O_2 activation without external stimulation, the reaction pathways follow two processes (**Figure 13**) based on the chemistry properties of various organics in aqueous solution. For the first approach, organics ionize into anionic/cation organic ions in aqueous solution and the following step is the adsorption process between catalysts and ionized organic ions either by chemical adsorption or electrostatic adsorption. Electron transferring occurs during this process, in which the electrons would be donated by the absorbed organic ions and delivered by perovskite catalysts to the dissolved oxygen molecule which acts as electron acceptor. Specifically, the electron delivery or migration process in perovskite oxides is proceeded via the $B^{n+}-O-B^{(n+1)+}$ network and valence alternation of B-site metals. After experiencing the main step, oxygen can be activated, and then ROS ($^{\cdot}OH$ and $^1O_2$) with high oxidation potential would be generated to react with organic ions for further degradation and mineralization. Another process is related to the azo dyes degradation. The initial step is the adsorption of azo dye molecules

by catalysts. Then azo bond of dyes breaks and passes one electron to the catalysts. Catalysts act as bridge to deliver electrons to activate oxygen adsorbates. The following reaction follows similar steps as the first kind of reaction mechanism. It is worth noting that for both processes, the electron-donating and transfer steps play key roles for the whole process because the following reaction process is triggered by the electron-donating and transfer. However, electrons from the pollutants are extremely limited, which is not sufficient for oxygen activation. This would further retard the ROS generation and lead to a relatively lower removal efficiency compared with the Fenton system and sulfate radical-based system. The adsorption process is also a key factor for the oxygen activation process to facilitate the adsorption process since the interaction among organics, oxygen, and catalysts are achieved by adsorption. Consequently, the degradation selectivity towards different organics is related to the surface properties of perovskite.

3.6. Perovskite Oxides in Catalytic Wet Air/Peroxide Oxidation

Wet oxidation process has been extensively investigated as it appeared to be an effective approach for high concentration refractory contaminants degradation. Unfortunately, the drawback of high-energy consumption due to the severe operation conditions (200–320 °C, 20–200 bar) retards their application.[89] Recently, heterogeneous catalytic wet air/peroxide oxidation serves as an alternative approach for these robust contaminations elimination due to the merits of eco-friendly and less energy requirement.[191] With the aid of solid catalysts and peroxide (H_2O_2), CWAO/peroxidation is an effective solution for refractory pollutants degradation since it can be operated in mild conditions (<100 °C and at atmospheric pressure).[192,193] Attempts have been devoted to developing high-efficiency heterogeneous catalysts for this process, like metal oxides, carbonaceous, noble metal supported on oxides as well as perovskite oxides.[87,191,194–197] This subsection will give a summarization and identification of major factors among numerous perovskite oxides served as heterogeneous catalysts for CWAO and CWPO process.

3.6.1. Effects of Surface Properties

Lanthanum-based perovskite oxides have been employed for the CWAO process.[198–203] In 2007, $LaFeO_3$ was utilized by Yang and co-workers in CWAO for salicylic acid (SA) oxidation.[198] They revealed that various adsorption behaviors between organic substances and catalyst surface govern the removal efficiency. H-bonding formation from chemical adsorption between SA molecules and basic centers of oxygen on the surface could facilitate the oxidation efficiency, but which is depending on the reaction temperature. A too high temperature would affect the organics structure (i.e., breaking the intramolecular H-bonding), thus leading to adverse impact for pollutants degradation. Therefore, in case of SA removal, the optimal reaction temperature would be around 140 °C. Electrostatic adsorption also helps the organic decomposition efficiency with typical examples of dyes degradation by perovskite
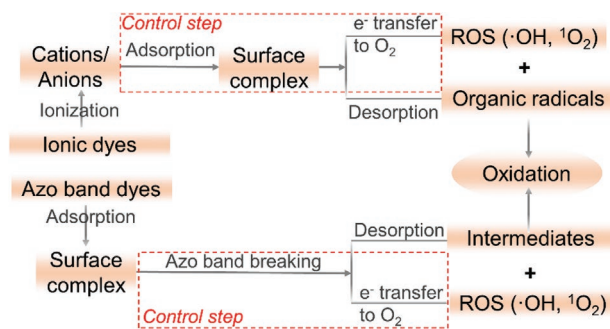
Figure 13. The schematic of dyes (ionic dyes and azo band dyes) decomposition pathways over perovskite oxides without energy input.

**ADVANCED
SCIENCE NEWS**

www.advancedsciencenews.com

**ADVANCED
FUNCTIONAL
MATERIALS**

www.afm-journal.de
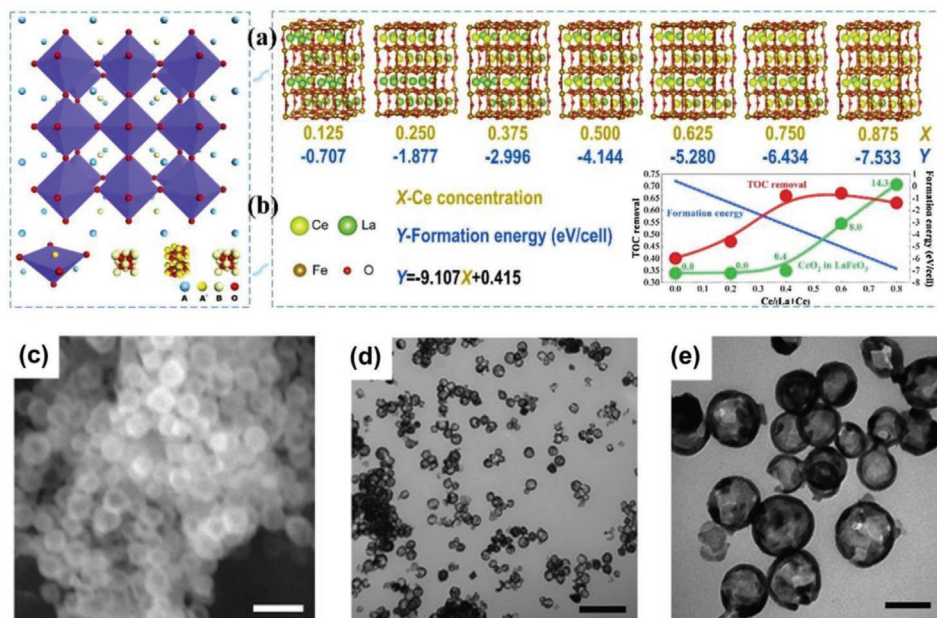
Figure 14. a) The supercells of Ce-doped LaFeO₃. b) The oxygen vacancy formation energy and TOC removal profiles versus Ce concentration. Reproduced with permission.[205] Copyright 2018, Elsevier. c–e) The morphology of LaMnO₃ hollow nanoparticles. The scale bar in TEM image (c) and SEM images (d,e) are 100, 500, and 50 nm, respectively. Reproduced with permission.[201] Copyright 2012, Elsevier.

oxide supported CWAO due to the positive/negative charged catalyst surface.[203] Apart from the organic adsorption, oxygen adsorption on catalyst surface would promote the ROS generation and degradation reaction.[204] To be more specific, gaseous oxygen can be absorbed on the B-site cations with lower valence (i.e., Co^{2+} and Mn^{3+}) which can donate electrons for O_2 activation to produce surface oxygen species. Thus $LaCoO_{3-\delta}$ with higher concentration of Co^{2+} possessed stronger oxygen storage capacity than $LaMnO_{3+\delta}$ with relatively lower concentration of Mn^{3+}. This kind of oxygen storage capacity exhibited a good correlation with the catalytic activity of CWAO. In spite of the fast degradation rate at the initial stage, $LaCoO_{3-\delta}$ can only achieve 65% mineralization due to the catalyst deactivation caused by carbonate accumulation on surface. In addition, a recent report has demonstrated that surface oxygen species and high valence surface iron atom (Fe^{3+}) can be regarded as the active sites for direct oxidation of organics.[205]

For CWPO process, both H_2O_2 activation and organic oxidation process are governed by the perovskite oxide surface features.[206] The mechanism of H_2O_2 decomposition and ·OH/HO₂· generation was advised to occur over B-site $M^{(n+1)+}$ active center by adsorption and subsequent electron transferring process. Moreover, competitive quenching tests verified that the surface bonded hydroxyl radicals were mainly responsible for the attack of organic molecules, instead of the free ·OH in the bulk solution.

3.6.2. Bulk Composition Tailoring

A series of $La_{1-x}Ce_xFeO_{3-\delta}$ perovskite oxides prepared by doping strategy to incorporate Ce into A-site of $LaFeO_{3-\delta}$ to investigate the electron structure change, CWAO efficiency,

and stability.[205] Experimental data showed that the incorporation of Ce into the skeleton has notable effects on the oxidation state of Fe, surface oxygen species, oxygen defect content, and catalyst stability. The first principle calculation presented that a higher Ce doping concentration favors defect generation owing to the reduced formation energy. As shown in **Figure 14**a,b, the organic removal efficiency was enhanced by the increased dopant content to form more oxygen defects as the active species for oxygen activation and ROS (O*) generation. Besides, the dramatic enhancement of stability with reduced metal leaching by Ce-doping was attributed to the strong overlap peaks of spin-down state around 0.5 eV over Fermi level for Ce-doped materials, while the strong overlap of Fe d band and O 2p band suggested that charge transfer between Fe—O would be facilitated. Generally, the electron conduction path of perovskite oxide follows the Zerner double exchange process in the catalytic reaction.[16,207] Thus the significantly enhanced electron transfer would help the activation of oxygen. Patricia et al. also confirmed the vital role of A-site foreign element doping effects in terms of catalytic activity and stability.[98] With the partial substitution of La in $LaFeO_3$ by Ti, an optimal activity with complete mineralization and, more importantly, higher stability with lower than 1% of Fe loss was achieved.

Lanthanum-based perovskite oxides containing various TMs have also been used for wet peroxide oxidation (CWPO) of phenol under mild conditions (**Table 6**).[186] Cu-containing catalysts possessed great potential for catalyzing H_2O_2 to produce ·OH in phenol oxidation, while $LaFeO_3$ exhibited strong stability. However, perovskites with Co, Ni, and Mn in B-site were inactive for CWPO. This feature is quite different from the sulfate radical-based AOPs, where Co is the most active component in perovskite oxides among numerous cations.[65,145] Interestingly, despite the inertness of $LaCoO_3$, an obvious

Table 6. Catalytic activity of selected perovskite oxide catalysts for catalytic wet air/peroxide oxidation.

Catalyst	Organic pollutants	Catalyst loading	Reaction condition	H_2O_2 dosage	Degradation efficiency	TOC removal	Metal leaching	Ref.
$LaFeO_3$	Salicylic acid [2000 ppm]	8 g L^{-1}	140 °C, 2.5 MPa	–	84%	–	15.6 ppm	[198]
$LaMnO_3$	Phenol [1000 ppm]	4 g L^{-1}	140 °C, 0.4 MPa	–	95% at 2 h	70% at 2 h	1.41 ppm	[201]
$LaNiO_3$	Reactive black 5 [100 ppm]	1 g L^{-1}	50 °C, 1 atm	–	65.4% at 2 h	33% at 2 h	–	[203]
$LaCoO_{3-\delta}$	Stearic acid [5625 ppm]	4 g L^{-1}	200 °C, 2 MPa	–	–	65% at 20 min	<0.2 g L^{-1}	[204]
$LaMnO_{3+\delta}$	Stearic acid [5625 ppm]	4 g L^{-1}	200 °C, 2 MPa	–	–	40.5% at 20 min		
$La_{0.4}Ce_{0.6}FeO_3$	Acrylic acid [10 g L^{-1}]	1 g L^{-1}	240 °C, 2 MPa	–	≈80% at 2 h	≈66% at 2 h	6 ppm	[205]
$La_{0.8}K_{0.2}FeO_3$	MB [500 ppm]	1 g L^{-1}	20 °C, ambient pressure	–	≈85% at 60 min	–	–	[209]
$LaCuO_3$	Phenol [0.01 $_M$]	5 g L^{-1}	30 °C, ambient pressure	0.7 $_M$	≈100% at 2.2 h	≈86% at 2.2 h	21.9 ppm at pH3	[186]
$LaFeO_3$	Phenol [0.01 $_M$]	5 g L^{-1}	30 °C, ambient pressure	0.7 $_M$	≈80% at 2.2 h	≈33% at 11 h	5.2 ppm at pH3	
$LaFeO_3$	Phenol [0.5 m$_M$]	1 g L^{-1}	25 °C, ambient pressure	0.1 $_M$	–	76% at 2 h	2.7 ppm	[200]
CeO_2-$LaCuO_3$	Bisphenol-F [20 ppm]	0.2 g L^{-1}	25 °C, ambient pressure	10 m$_M$	100% at 45 min	82.43% at 6 h	0.98 ppm at pH3	[206]
$PrFe_{0.8}Co_{0.2}O_3$	Salicylic acid [100 ppm]	20 mg L^{-1}	100 °C, ambient pressure	1.2 mL L^{-1}	91% at 1 h	–	–	[208]
Ti-doped $LaFeO_3$	4-CP [25 ppm]	0.5 g L^{-1}	25 °C, ambient pressure	125 mg L^{-1}	–	100% at 6 h	<0.2 ppm	[210]

improvement of organic removal was achieved by Co doping in $LaFeO_3$ and $PrFeO_3$ for 2-Hydroxybenzoic acid elimination in CWPO.[208] Such an enhancement might be attributed to the synergistic effects between dopants and parent transitional cations.
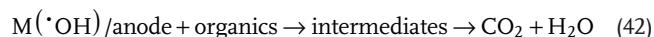
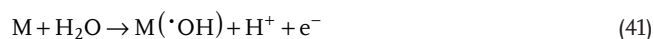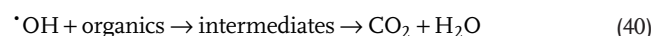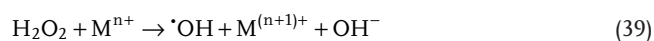### 3.6.3. Surfacing Engineering and Morphology Control

In order to avoid agglomeration and increase the surface area, a urea-assisted approach was used to prepare $LaMnO_3$ hollow nanoparticles (Figure 14c–e).[201] With the aid of urea, the rates of nucleation, precipitation, and agglomeration were reduced and thus yielded hollow nanosphere particles with high surface area (31 m^2 g^{-1}) and improved CWAO efficiency for phenol decomposition. Comparing to the conventional catalysts with lower surface area which only achieved 70% TOC abatement, the nano-hollow structured perovskites can reach 95% mineralization in 2 h with ignorable Mn leaching.

Another porous perovskite $La_{0.8}K_{0.2}FeO_3$ in hollow microfiber structure with microchannels was developed for MB removal in CWAO under ambient conditions.[209] Benefiting from the relatively high surface area (17.56 m^2 g^{-1}) and pore volume provided by the mesoporous structure, the hollow microfiber gave high decolorization efficiency, and lower activation energy (14.27 kJ mol^{-1}). Faye et al. used combustion method to synthesize the $LaFeO_3$ by varying the ratio of glycine/NO_3^-, which has obvious influence on the textural properties of catalysts.[200] At the ratio of 1, the prepared $LaFeO_3$ (crystal size of 28 nm) had a surface area of 19.9 m^2 g^{-1} larger than other samples and thus contributed to the effective catalytic peroxidation process. Similar results have been achieved by Hammouda et al. who synthesized ceria-perovskite oxides composites via a facile sintering combination method for CWPO.[206] The boosted activity of the nanoperovksite composite catalysts was mainly sourced from the enlarged surface area as well as the synergistic effects of cerium and transitional metal cations.

3.7. Perovskite Oxides in Electrochemical AOPs (EAOPs)

Among these emerging new technologies for water remediation, EAOPs also known as electron-assisted AOPs have been recently studied as a novel advanced technique to eliminate some noxiously persistent organic pollutants. In this process, the organic removal is achieved mainly by the means of in situ generated ROS and anodic oxidations.[210] Coupling the synergistic effects from the two processes. Several papers reported such an electron-assisted process using carbon/transitional metal oxide-based anodes for efficient organic degradation.[89,211–214] Hammouda developed a heterogeneous electron-Fenton system by simply integrating in situ and electrocatalytic H_2O_2 generation using double Sr_2FeCuO_6 catalyst for aqueous contaminant oxidation, where born-doped diamond and carbon belt were used as the respective anode and cathode.[174] Upon the applied current density of 8 mA cm^{-2} and continuous O_2 blowing, the aqueous cotinine (50 ppm, 0.5 L) was almost completed mineralized in 8 h at acid media, indicating the strong and durable oxidation capacity of the EAOPs. The EAOPs process is far more complicated than the single AOPs since the reaction is initiated by the oxygen reduction reaction (ORR) on cathode. Nevertheless, different from the traditional ORR, the two-electron transfer process (Equation (38)) for H_2O_2 in situ generation is a more desirable reaction on cathode rather than the four-electron transfer process. Carbon belt without any modification favors the 2-electron transfer process and thus enhances the in situ generation of H_2O_2, which immediately diffuses into bulk phase and is activated subsequently over the Sr_2FeCuO_6 perovskite for $^\cdot OH$ production and organics oxidation (Equation (39,40)). Simultaneously, both of the surface active sites bonded hydroxyl radicals M($^\cdot OH$) formed on anode through oxidation of H_2O and direct anode oxidation of organics contribute to the high elimination efficiency (Equation (41,42)). However, the control step of the EAOPs should be the ORR on the cathode. Therefore, rational design or optimization of cathode could improve the

ADVANCED
SCIENCE NEWS
www.advancedsciencenews.com

ADVANCED
FUNCTIONAL
MATERIALS
www.afm-journal.de

degradation efficiency fundamentally. For example, in order to promote the mass-transfer efficiency of ORR on cathode, Wang et al. prepared a $La_{1-x}Nd_xFeO_3$ air diffusion cathode with a plate shape (3×5 cm^2) for the MO degradation.[215] The most efficient $La_{0.6}Nd_{0.4}FeO_3$ exhibited a 99.81% decolor rate in 10 min at 4 mA cm^{-2}, mirroring the good oxidative property of the cathode. Identically, the degradation processes are also composed of the ORR on cathode, the H_2O_2 activation via Fenton reaction, and MO decomposition through both $^\bullet$OH and anode oxidation.

$$O_2(g) + 2H^+ + 2e^- \rightarrow H_2O_2 \tag{38}$$

$$H_2O_2 + M^{n+} \rightarrow {}^\bullet OH + M^{(n+1)+} + OH^- \tag{39}$$

$${}^\bullet OH + organics \rightarrow intermediates \rightarrow CO_2 + H_2O \tag{40}$$

$$M + H_2O \rightarrow M({}^\bullet OH) + H^+ + e^- \tag{41}$$

$$M({}^\bullet OH)/anode + organics \rightarrow intermediates \rightarrow CO_2 + H_2O \tag{42}$$

4. Conclusions and Perspectives

Perovskite oxides have demonstrated interesting applications for peroxides activation in AOPs. In this article, the recent progress of catalytic activation of various peroxides and photocatalysis for organic oxidation or removal by perovskite oxides has been comprehensively reviewed. Noteworthy that the overall catalytic efficiency of AOPs does not rely on one single factor, instead, is quite dependent on the intrinsic catalyst properties and operating conditions. Due to the different reaction systems of these various AOPs, it is difficult to draw a universal or straightforward design principle to suit all the catalysts. However, there are some general guidelines for catalyst design to follow in a sequence of bulk composition regulation, surface modification, hybrids construction, and engineering considerations.

4.1. Compositional Regulation

Considering the property-activity relationship of different AOP systems and taking the advantage of compositional flexibility from perovskite oxides, a verity of elements can be accommodated into A-, B- and/or O-site, thus allowing the facile tailoring of properties to achieve outstanding catalytic activity. In AOPs, despite many other factors, catalytic activity mainly originates from the B-site transitional metals. For instance, for H_2O_2 activation in Fenton, photo/photo-Fenton, and wet air/peroxide oxidation process, Fe-containing perovskites exhibit the most promising performance followed by Cu, Ti, and Al. By contrast, perovskites with Co are the most efficient catalysts for PMS activation and the activity follows the order of Co > Ni > Cu > Fe in La-based perovskite. In catalytic ozonation process, Mn-based perovskites demonstrate higher activity than Fe

and Ti-based perovskite; while in catalytic wet air/peroxide process, Cu-containing perovskites exhibit announced activities. In addition to the host element selection, foreign elements, either are redox-active or redox-inactive, doping at B-site can cause significant effects. The incorporation of catalytically active dopants in suitable amounts, like Fe, Cu, and Mn can synergistically improve the peroxide activation kinetics via forming conjunctive redox couples. On the other hand, the introduction of redox-inactive dopants such as Ti and Zr at B-site can affect the electronic environment of the adjacent catalytic active centers and thus improve the activity and stability. For example, Ti-doped $SrCoO_3$ perovskite gives great optimal activity and stability in PMS activation.

In comparison with B-site, A-site inert elements function in indirect approaches. In general, the properties of dopants (i.e., alkalinity/acidity, valence, atomic radius, and electronic structure) have strong impacts on the surface properties, defects content, electron structure, and B-site oxidation states. Additionally, according to the molecular orbital theory that e_g orbital filling number seems to be a suitable activity descriptor for PMS activation, the types and the amounts of dopants at both A- and B-site can be optimized to give rise to an optimal electronic configuration. In addition, anion doping at O-site is mainly applied in semiconductors for adjusting VB position to minimize the bandgap energy and enhance the charge carriers separation ability. But so far, limited anion elements have been investigated for O-site doping for peroxide activation.

In brief, since the first application of perovskite oxides in AOPs, tremendous works have been done to explore the most efficient candidates via compositional control, but some challenges are still existing. For example, the trade-off generally exists between the activity and stability (metal leaching problem), especially for Co-based perovskite. Moreover, the aforementioned observations are mostly based on empirical results. Therefore, a deeper understanding of the intrinsic structure-activity relationship and a more systematic study for probing the determining factors of perovskite activity in AOPs are of scientific importance, which could guide the design and development of perovskite-based catalysts for AOPs.

4.2. Surface Modification

The good surface interaction between perovskite oxides and peroxide molecules is the prerequisite to achieve the ideal activity. In particular, surface properties play more important roles in catalytic ozonation and O_2 activation processes because they involve three-phase (gas, liquid, and solid) reactions, where the mass transfer is the key stage of activation and ROS evolution. Firstly, surface modification by the in situ formation of ligands using organic chelating agents (i.e., tartaric, formic acid, and EDTA) to accelerate the interaction of reactant molecules with catalysts. Secondly, tailoring surface charging states or functional groups of perovskite oxides by nanocasting or post-treatment can favor the adsorption of peroxides and organics via electronic or H-bonding, which could also lead to improvement. Thirdly, specific active facet exposure by facet engineering and morphology control can boost the ROS generation efficiency. Lastly, enlarging specific surface area and

**ADVANCED
SCIENCE NEWS**

www.advancedsciencenews.com

**ADVANCED
FUNCTIONAL
MATERIALS**

www.afm-journal.de

porosity of perovskite oxides would enhance the adsorption and expose more active sites.

4.3. Constructing Heterostructure

The purpose of constructing composites is to integrate the multiple functional characters from each individual compound. In regarding the perovskite oxides, compositing a second phase demonstrates a promising way to overcome the drawbacks of large particle size, low specific surface area, and inferior charge transfer capacity. One potential candidate for compositing is carbon materials. Through incorporating 2D carbon materials, the most distinguishing property of the hybrids is the capability to improve the electron conductivity, which thus yields a high separation capacity of photo-induced charge carriers. However, studies are rarely performed to develop the perovskite/carbon hybrids in the peroxide-based AOPs. The main reason might be the difficulty in maintaining the skeleton of perovskite oxide in the compositing process with carbonaceous materials. Though attempts have been made in compositing via physical methods, efforts are still required for engineering more compact hybrids with intimate interface. Moreover, borrowing the insights obtained from the well-developed electrochemical systems, that is, preparing multi-structure compounds like single/layered perovskite hybrids via solid solution or self-assembling approaches, would generate a wider range of properties than each of the single compound.

4.4. Engineering Considerations

Oxygen defects (oxygen vacancy and oxygen excess) are fascinating features of perovskite oxides and are identified as active sites for peroxides adsorption and activation. In perovskite/PMS system, it is speculated that the oxygen vacancy is more likely to be the adsorption site in the radical generation process while it is proved to be the most active site in catalytic ozonation. Thus, oxygen defect creation via a variety of techniques would assist the catalytic performance. In addition to the aforementioned aliovalent/isovalent doping, other engineering methods like cation defects creation, increasing surface areas, porosity, or post-treatment in reduced or oxidative gas atmosphere under high temperatures can also be applied to create excess oxygen or oxygen vacancies and expose these active sites for more efficient reactions. Moreover, despite the positive correlation between the catalytic activity of perovskite oxides and the number of oxygen defects created has verified the indispensable role of oxygen defects in AOPs, the fundamental understanding of how oxygen vacancy interacts with peroxides in the activation process still remains vague. To tackle this problem, combined techniques including the operando experimental/characterization and theoretical calculation are important. Particularly, the in situ observation of peroxide molecule decomposition on surface oxygen vacancy site would help to understand the oxygen vacancy evolution process from surface to bulk or vice versa.

To conclude, perovskite oxides are experiencing unprecedented development in the applications of AOPs. The favorable features delivered by perovskite oxides are captured more and more researchers imagination. The structural and composi-

tional flexibility endow them very rich properties, such as ferromagnetic property, piezoelectricity, and superconductivity, providing great opportunities for their further applications in the areas of energy conversion and environmental remediation.

Conflict of Interest

The authors declare no conflict of interest.

Data Availability Statement

The data that support the findings of this study are available from the corresponding authors upon reasonable request.

[1] X. Duan, H. Sun, S. Wang, *Acc. Chem. Res.* **2018**, *51*, 678.

[2] F. Li, D. Lin, Z. Chen, Z. Cheng, J. Wang, C. Li, Z. Xu, Q. Huang, X. Liao, L.-Q. Chen, T. R. Shrout, S. Zhang, *Nat. Mater.* **2018**, *17*, 349.

[3] F. Mushtaq, X. Chen, H. Torlakcik, C. Steuer, M. Hoop, E. C. Siringil, X. Marti, G. Limburg, P. Stipp, B. J. Nelson, S. Pané, *Nat. Mater.* **2019**, *31*, 1901378.

[4] Y. Zhu, Q. Lin, Z. Hu, Y. Chen, Y. Yin, H. A. Tahini, H.-J. Lin, C.-T. Chen, X. Zhang, Z. Shao, H. Wang, *Small* **2020**, *16*, 2001204.

[5] Y. Pan, X. Xu, Y. Zhong, L. Ge, Y. Chen, J.-P. M. Veder, D. Guan, R. O'Hayre, M. Li, G. Wang, H. Wang, W. Zhou, Z. Shao, *Nat. Commun.* **2020**, *11*, 2002.

[6] X. Liang, L. Shi, R. Cao, G. Wan, W. Yan, H. Chen, Y. Liu, X. Zou, *Adv. Mater.* **2020**, *32*, 2001430.

[7] X. Miao, L. Zhang, L. Wu, Z. Hu, L. Shi, S. Zhou, *Nat. Commun.* **2019**, *10*, 3809.

[8] W. Wang, M. Xu, X. Xu, W. Zhou, Z. Shao, *Angew. Chem., Int. Ed.* **2020**, *59*, 136.

[9] S. Royer, D. Duprez, F. Can, X. Courtois, C. Batiot-Dupeyrat, S. Laassiri, H. Alamdari, *Chem. Rev.* **2014**, *114*, 10292.

[10] W.-J. Yin, B. Weng, J. Ge, Q. Sun, Z. Li, Y. Yan, *Energy Environ. Sci.* **2019**, *12*, 442.

[11] A. Kumar, A. Kumar, V. Krishnan, *ACS Catal.* **2020**, *10*, 10253.

[12] R. Ubic, K. Tolman, K. Talley, B. Joshi, J. Schmidt, E. Faulkner, J. Owens, M. Papac, A. Garland, C. Rumrill, K. Chan, N. Lundy, H. Kungl, *J. Alloys Compd.* **2015**, *644*, 982.

[13] W. Li, E. Ionescu, R. Riedel, A. Gurlo, *J. Mater. Chem. A* **2013**, *1*, 12239.

[14] R. Ubic, K. Tolman, K. Chan, N. Lundy, S. Letourneau, W. M. Kriven, *J. Alloys Compd.* **2013**, *575*, 239.

[15] C. Zhang, J. Sunarso, S. Liu, *Chem. Soc. Rev.* **2017**, *46*, 2941.

[16] S. Sengodan, S. Choi, A. Jun, T. H. Shin, Y.-W. Ju, H. Y. Jeong, J. Shin, J. T. S. Irvine, G. Kim, *Nat. Mater.* **2014**, *14*, 205.

[17] M. Osada, T. Sasaki, *Dalton Trans.* **2018**, *47*, 2841.

[18] G. King, P. M. Woodward, *J. Mater. Chem.* **2010**, *20*, 5785.

[19] W.-t. Chen, M. Mizumaki, H. Seki, M. S. Senn, T. Saito, D. Kan, J. P. Attfield, Y. Shimakawa, *Nat. Commun.* **2014**, *5*, 3909.

[20] Y. Zhu, H. A. Tahini, Z. Hu, J. Dai, Y. Chen, H. Sun, W. Zhou, M. Liu, S. C. Smith, H. Wang, Z. Shao, *Nat. Commun.* **2019**, *10*, 149.

[21] J. Gopalakrishnan, T. Sivakumar, K. Ramesha, V. Thangadurai, G. N. Subbanna, *J. Am. Chem. Soc.* **2000**, *122*, 6237.

[22] J. Yu, J. Sunarso, Y. Zhu, X. Xu, R. Ran, W. Zhou, Z. Shao, *Chem. - Eur. J.* **2016**, *22*, 2719.

[23] H. Lv, L. Lin, X. Zhang, Y. Song, H. Matsumoto, C. Zeng, N. Ta, W. Liu, D. Gao, G. Wang, X. Bao, *Adv. Mater.* **2020**, *32*, 1906193.

[24] Y. Wang, Z. Chi, C. Chen, C. Su, D. Liu, Y. Liu, X. Duan, S. Wang, *Appl. Catal., B* **2020**, *272*, 118972.

[25] L. Ge, W. Zhou, R. Ran, S. Liu, Z. Shao, W. Jin, N. Xu, *J. Membr. Sci.* **2007**, *306*, 318.

[26] M. Wehrens-Dijksma, P. H. L. Notten, *Electrochim. Acta* **2006**, *51*, 3609.

[27] C. Su, X. Duan, J. Miao, Y. Zhong, W. Zhou, S. Wang, Z. Shao, *ACS Catal.* **2017**, *7*, 388.

[28] A. Demont, S. Abanades, *J. Mater. Chem. A* **2015**, *3*, 3536.

[29] S. Irusta, M. P. Pina, M. Menéndez, J. Santamaría, *J. Catal.* **1998**, *179*, 400.

[30] Y. Sun, J. Li, Y. Zeng, B. S. Amirkhiz, M. Wang, Y. Behnamian, J. Luo, *J. Mater. Chem. A* **2015**, *3*, 11048.

[31] G. P. Anipsitakis, D. D. Dionysiou, *Environ. Sci. Technol.* **2004**, *38*, 3705.

[32] S. Lu, G. Wang, S. Chen, H. Yu, F. Ye, X. Quan, *J. Hazard. Mater.* **2018**, *353*, 401.

[33] D. N. Mueller, M. L. Machala, H. Bluhm, W. C. Chueh, *Nat. Commun.* **2015**, *6*, 6097.

[34] H. B. Tao, J. Zhang, J. Chen, L. Zhang, Y. Xu, J. G. Chen, B. Liu, *J. Am. Chem. Soc.* **2019**, *141*, 13803.

[35] V. V. Kharton, I. P. Marozau, N. P. Vyshatko, A. L. Shaula, A. P. Viskup, E. N. Naumovich, F. M. B. Marques, *Mater. Res. Bull.* **2003**, *38*, 773.

[36] C. Mao, H. Cheng, H. Tian, H. Li, W.-J. Xiao, H. Xu, J. Zhao, L. Zhang, *Appl. Catal., B* **2018**, *228*, 87.

[37] D. D. Cuong, B. Lee, K. M. Choi, H.-S. Ahn, S. Han, J. Lee, *Phys. Rev. Lett.* **2007**, *98*, 115503.

[38] J. Kim, X. Yin, K.-C. Tsao, S. Fang, H. Yang, *J. Am. Chem. Soc.* **2014**, *136*, 14646.

[39] Q. Ji, L. Bi, J. Zhang, H. Cao, X. S. Zhao, *Energy Environ. Sci.* **2020**, *13*, 1408.

[40] S. She, J. Yu, W. Tang, Y. Zhu, Y. Chen, J. Sunarso, W. Zhou, Z. Shao, *ACS Appl. Mater. Interfaces* **2018**, *10*, 11715.

[41] W. Wang, Y. Yang, D. Huan, L. Wang, N. Shi, Y. Xie, C. Xia, R. Peng, Y. Lu, *J. Mater. Chem. A* **2019**, *7*, 12538.

[42] J. Miao, J. Sunarso, C. Su, W. Zhou, S. Wang, Z. Shao, *Sci. Rep.* **2017**, *7*, 44215.

[43] Y. Wang, L. Chen, H. Cao, Z. Chi, C. Chen, X. Duan, Y. Xie, F. Qi, W. Song, J. Liu, S. Wang, *Appl. Catal., B* **2019**, *245*, 546.

[44] W. Xie, Y.-L. Lee, Y. Shao-Horn, D. Morgan, *J. Phys. Chem. Lett.* **2016**, *7*, 1939.

[45] J. W. Han, B. Yildiz, *Energy Environ. Sci.* **2012**, *5*, 8598.

[46] D.-S. Byeon, S.-M. Jeong, K.-J. Hwang, M.-Y. Yoon, H.-J. Hwang, S. Kim, H.-L. Lee, *J. Power Sources* **2013**, *222*, 282.

[47] S. P. Jiang, L. Liu, K. P. Ong, P. Wu, J. Li, J. Pu, *J. Power Sources* **2008**, *176*, 82.

[48] L. Zhang, Y. Nie, C. Hu, J. Qu, *Appl. Catal., B* **2012**, *125*, 418.

[49] L. Gan, Q. Zhong, X. Zhao, Y. Song, Y. Bu, *J. Alloys Compd.* **2016**, *655*, 99.

[50] M. Liu, L. zhao, D. Dong, S. Wang, J. Diwu, X. Liu, G. Meng, *J. Power Sources* **2008**, *177*, 451.

[51] Y. Zhu, W. Zhou, J. Yu, Y. Chen, M. Liu, Z. Shao, *Chem. Mater.* **2016**, *28*, 1691.

[52] Y. Zhu, Z.-G. Chen, W. Zhou, S. Jiang, J. Zou, Z. Shao, *ChemSusChem* **2013**, *6*, 2249.

[53] Z. Teng, Z. Xiao, G. Yang, L. Guo, X. Yang, R. Ran, W. Wang, W. Zhou, Z. Shao, *Mater. Today Energy* **2020**, *17*, 100458.

[54] A. Gómez-Pérez, M. T. Azcondo, M. Yuste, J. C. Pérez-Flores, N. Bonanos, F. Porcher, A. Muñoz-Noval, M. Hoelzel, F. García-Alvarado, U. Amador, *J. Mater. Chem. A* **2016**, *4*, 3386.

[55] Y. Zhu, Y. Lin, X. Shen, J. Sunarso, W. Zhou, S. Jiang, D. Su, F. Chen, Z. Shao, *RSC Adv.* **2014**, *4*, 40865.

[56] X. Zhu, K. Li, L. Neal, F. Li, *ACS Catal.* **2018**, *8*, 8213.

[57] F. V. E. Hensling, D. J. Keeble, J. Zhu, S. Brose, C. Xu, F. Gunkel, S. Danyluk, S. S. Nonnenmann, W. Egger, R. Dittmann, *Sci. Rep.* **2018**, *8*, 8846.

[58] G. Guo, K. Ouyang, J. Yu, Y. Liu, S. Feng, M. Wei, *ACS Appl. Energy Mater.* **2020**, *3*, 300.

[59] J. Mizusaki, N. Mori, H. Takai, Y. Yonemura, H. Minamiue, H. Tagawa, M. Dokiya, H. Inaba, K. Naraya, T. Sasamoto, T. Hashimoto, *Solid State Ion* **2000**, *129*, 163.

[60] J. T. Mefford, W. G. Hardin, S. Dai, K. P. Johnston, K. J. Stevenson, *Nat. Mater.* **2014**, *13*, 726.

[61] K. Nakamura, K. Ogawa, *J. Appl. Phys.* **2002**, *92*, 6684.

[62] J. Miao, J. Li, J. Dai, D. Guan, C. Zhou, W. Zhou, X. Duan, S. Wang, Z. Shao, *Ind. Eng. Chem. Res.* **2019**, *59*, 99.

[63] J. Suntivich, K. J. May, H. A. Gasteiger, J. B. Goodenough, Y. Shao-Horn, *Science* **2011**, *334*, 1383.

[64] J. Suntivich, H. A. Gasteiger, N. Yabuuchi, H. Nakanishi, J. B. Goodenough, Y. Shao-Horn, *Nat. Chem.* **2011**, *3*, 546.

[65] J. Miao, J. Sunarso, X. Duan, W. Zhou, S. Wang, Z. Shao, *J. Hazard. Mater.* **2018**, *349*, 177.

[66] P. Zeng, Z. Shao, S. Liu, Z. P. Xu, *Sep. Purif. Technol.* **2009**, *67*, 304.

[67] A. Leo, S. Liu, J. C. Diniz da Costa, *J. Membr. Sci.* **2009**, *340*, 148.

[68] Y. Song, Y. Chen, W. Wang, C. Zhou, Y. Zhong, G. Yang, W. Zhou, M. Liu, Z. Shao, *Joule* **2019**, *3*, 2842.

[69] M. A. Oturan, J.-J. Aaron, *Crit. Rev. Environ. Sci. Technol.* **2014**, *44*, 2577.

[70] P. Bautista, A. F. Mohedano, J. A. Casas, J. A. Zazo, J. J. Rodriguez, *J. Chem. Technol. Biotechnol.* **2008**, *83*, 1323.

[71] L. Lyu, D. Yan, G. Yu, W. Cao, C. Hu, *Environ. Sci. Technol.* **2018**, *52*, 4294.

[72] N. Wang, T. Zheng, G. Zhang, P. Wang, *J. Environ. Chem. Eng.* **2016**, *4*, 762.

[73] N. A. Zubir, C. Yacou, J. Motuzas, X. Zhang, J. C. Diniz da Costa, *Sci. Rep.* **2014**, *4*, 4594.

[74] D. Li, H. Zhao, L. Li, B. Mao, M. Chen, H. Shen, W. Shi, D. Jiang, Y. Lei, *Adv. Funct. Mater.* **2018**, *0*, 1806284.

[75] W. Wang, M. O. Tadé, Z. Shao, *Chem. Soc. Rev.* **2015**, *44*, 5371.

[76] X. Duan, C. Su, L. Zhou, H. Sun, A. Suvorova, T. Odedairo, Z. Zhu, Z. Shao, S. Wang, *Appl. Catal., B* **2016**, *194*, 7.

[77] J. Lee, U. von Gunten, J.-H. Kim, *Environ. Sci. Technol.* **2020**, *54*, 3064.

[78] J. Wang, S. Wang, *Chem. Eng. J.* **2018**, *334*, 1502.

[79] Q. Dai, J. Wang, J. Yu, J. Chen, J. Chen, *Appl. Catal., B* **2014**, *144*, 686.

[80] Q. Dai, Z. Zhang, T. Zhan, Z.-T. Hu, J. Chen, *ACS Omega* **2018**, *3*, 6506.

[81] Q. Dai, L. Chen, S. Zhou, J. Chen, *RSC Adv.* **2015**, *5*, 24649.

[82] J. NawrockiB, *Appl. Catal., B* **2010**, *99*, 27.

[83] L. Zhao, Z. Sun, J. Ma, *Environ. Sci. Technol.* **2009**, *43*, 4157.

[84] J. Wang, Z. Bai, *Chem. Eng. J.* **2017**, *312*, 79.

[85] Z. Bai, Q. Yang, J. Wang, *Chemosphere* **2016**, *161*, 174.

[86] T. Zhang, J. Ma, *J. Mol. Catal. A: Chem.* **2008**, *279*, 82.

[87] A. Kumar, N. Verma, *Chem. Eng. J.* **2018**, *351*, 428.

[88] M. L. Tummino, E. Laurenti, F. Deganello, A. Bianco Prevot, G. Magnacca, *Appl. Catal., B* **2017**, *207*, 174.

[89] M. Sun, Y. Zhang, S.-Y. Kong, L.-F. Zhai, S. Wang, *Water Res.* **2019**, *158*, 313.

[90] M. K. Sushma, A. K. Saroha, *J. Environ. Manage.* **2018**, *228*, 169.

[91] H. Chen, J. Motuzas, W. Martens, J. C. Diniz da Costa, *Appl. Catal., B* **2018**, *221*, 691.

[92] W. Luo, L. Zhu, N. Wang, H. Tang, M. Cao, Y. She, *Environ. Sci. Technol.* **2010**, *44*, 1786.

[93] N. Wang, L. Zhu, M. Lei, Y. She, M. Cao, H. Tang, *ACS Catal.* **2011**, *1*, 1193.

[94] P. Xiao, J. Hong, T. Wang, X. Xu, Y. Yuan, J. Li, J. Zhu, *Catal. Lett.* **2013**, *143*, 887.

[95] K. Rusevova, R. Köferstein, M. Rosell, H. H. Richnow, F.-D. Kopinke, A. Georgi, *Chem. Eng. J.* **2014**, *239*, 322.

[96] Y. Nie, L. Zhang, Y.-Y. Li, C. Hu, *J. Hazard. Mater.* **2015**, *294*, 195.

[97] J. Li, J. Miao, X. Duan, J. Dai, Q. Liu, S. Wang, W. Zhou, Z. Shao, *Adv. Funct. Mater.* **2018**, *28*, 1804654.

[98] Y. Wang, H. Arandiyan, H. A. Tahini, J. Scott, X. Tan, H. Dai, J. D. Gale, A. L. Rohl, S. C. Smith, R. Amal, *Nat. Commun.* **2017**, *8*, 15553.

[99] Y. Liu, H. Dai, J. Deng, L. Zhang, B. Gao, Y. Wang, X. Li, S. Xie, G. Guo, *Appl. Catal., B* **2013**, *140–141*, 317.

[100] H. Zhao, J. Cao, H. Lv, Y. Wang, G. Zhao, *Catal. Commun.* **2013**, *41*, 87.

[101] S. Li, G. Zhang, H. Zheng, Y. Zheng, P. Wang, *Environ. Sci. Pollut. Res.* **2017**, *24*, 24400.

[102] S. Li, G. Zhang, H. Zheng, N. Wang, Y. Zheng, P. Wang, *RSC Adv.* **2016**, *6*, 82439.

[103] S. Li, G. Zhang, W. Zhang, H. Zheng, W. Zhu, N. Sun, Y. Zheng, P. Wang, *Chem. Eng. J.* **2017**, *326*, 756.

[104] J. Mao, X. Quan, J. Wang, C. Gao, S. Chen, H. Yu, Y. Zhang, *Front. Environ. Sci. Eng.* **2018**, *12*, 10.

[105] S. Jauhar, M. Dhiman, S. Bansal, S. Singhal, *J. Sol-Gel Sci. Technol.* **2015**, *75*, 124.

[106] M. R. Carrasco-Díaz, E. Castillejos-López, A. Cerpa-Naranjo, M. L. Rojas-Cervantes, *Chem. Eng. J.* **2016**, *304*, 408.

[107] H. Wang, L. Zhang, C. Hu, X. Wang, L. Lyu, G. Sheng, *Chem. Eng. J.* **2018**, *332*, 572.

[108] F. Gao, X. Y. Chen, K. B. Yin, S. Dong, Z. F. Ren, F. Yuan, T. Yu, Z. G. Zou, J. M. Liu, *Adv. Mater.* **2007**, *19*, 2889.

[109] T.-J. Park, G. C. Papaefthymiou, A. J. Viescas, A. R. Moodenbaugh, S. S. Wong, *Nano Lett.* **2007**, *7*, 766.

[110] R. Guo, L. Fang, W. Dong, F. Zheng, M. Shen, *J. Mater. Chem.* **2011**, *21*, 18645.

[111] L. Li, M. Zhang, P. Tian, W. Gu, X. Wang, *Ceram. Int.* **2014**, *40*, 13813.

[112] F.-t. Li, Y. Liu, R.-h. Liu, Z.-m. Sun, D.-s. Zhao, C.-g. Kou, *Mater. Lett.* **2010**, *64*, 223.

[113] T. Soltani, B.-K. Lee, *J. Mol. Catal. A: Chem.* **2016**, *425*, 199.

[114] W. Wang, M. O. Tadé, Z. Shao, *Prog. Mater. Sci.* **2018**, *92*, 33.

[115] M. Humayun, A. Qu, F. Raziq, R. Yan, Z. Li, X. Zhang, L. Jing, *Environ. Sci. Technol.* **2016**, *50*, 13600.

[116] M. P. Rao, V. P. Nandhini, J. J. Wu, A. Syed, F. Ameen, S. Anandan, *J. Solid State Chem.* **2018**, *258*, 647.

[117] Y. Jia, C. Wu, D.-H. Kim, B. W. Lee, S. J. Rhee, Y. C. Park, C. S. Kim, Q. J. Wang, C. Liu, *Chem. Eng. J.* **2018**, *337*, 709.

[118] G. Iervolino, V. Vaiano, D. Sannino, L. Rizzo, A. Galluzzi, M. Polichetti, G. Pepe, P. Campiglia, *Int. J. Hydrogen Energy* **2018**, *43*, 2184.

[119] T. T. N. Phan, A. N. Nikoloski, P. A. Bahri, D. Li, *J. Ind. Eng. Chem.* **2018**, *61*, 53.

[120] D. Wang, T. Kako, J. Ye, *J. Am. Chem. Soc.* **2008**, *130*, 2724.

[121] T. Soltani, B.-K. Lee, *Chem. Eng. J.* **2017**, *313*, 1258.

[122] P. R. Vanga, R. V. Mangalaraja, M. Ashok, *Mater. Res. Bull.* **2015**, *72*, 299.

[123] J. An, L. Zhu, Y. Zhang, H. Tang, *J. Environ. Sci.* **2013**, *25*, 1213.

[124] D. Sannino, V. Vaiano, P. Ciambelli, L. A. Isupova, *Chem. Eng. J.* **2013**, *224*, 53.

[125] R. Guo, L. Fang, W. Dong, F. Zheng, M. Shen, *J. Phys. Chem. C* **2010**, *114*, 21390.

[126] S. Mamidi, R. Gundeboina, S. Kurra, R. Velchuri, V. Muga, *C. R. Chim.* **2018**, *21*, 547.

[127] Z. Li, H. Xue, X. Wang, X. Fu, *J. Mol. Catal. A: Chem.* **2006**, *260*, 56.

[128] M. I. Zaki, W. Ramadan, A. Katrib, A. I. M. Rabee, *Appl. Surf. Sci.* **2014**, *317*, 929.

[129] J. Zhou, L. Jiang, D. Chen, J. Liang, L. Qin, L. Bai, X. Sun, Y. Huang, *J. Sol-Gel Sci. Technol.* **2019**, *90*, 535.

[130] Y. Soltanabadi, M. Jourshabani, Z. Shariatinia, *Sep. Purif. Technol.* **2018**, *202*, 227.

[131] Y. Ye, H. Yang, H. Zhang, J. Jiang, *Environ. Technol.* **2018**, *41*, 1.

[132] K. Peng, L. Fu, H. Yang, J. Ouyang, *Sci. Rep.* **2016**, *6*, 19723.

[133] J. An, G. Zhang, R. Zheng, P. Wang, *J. Environ. Sci.* **2016**, *48*, 218.

[134] R. Dhinesh Kumar, R. Thangappan, R. Jayavel, *J. Inorg. Organomet. Polym. Mater.* **2017**, *27*, 892.

[135] J. Ran, W. Guo, H. Wang, B. Zhu, J. Yu, S.-Z. Qiao, *Adv. Mater.* **2018**, *30*, 1800128.

[136] J. An, L. Zhu, N. Wang, Z. Song, Z. Yang, D. Du, H. Tang, *Chem. Eng. J.* **2013**, *219*, 225.

[137] D. Jiang, T. Wang, Q. Xu, D. Li, S. Meng, M. Chen, *Appl. Catal., B* **2017**, *201*, 617.

[138] Y. Ye, H. Yang, X. Wang, W. Feng, *Mater. Sci. Semicond. Process.* **2018**, *82*, 14.

[139] K. Wang, H. Niu, J. Chen, J. Song, C. Mao, S. Zhang, Y. Gao, *Appl. Surf. Sci.* **2017**, *404*, 138.

[140] Y. Wu, H. Wang, W. Tu, Y. Liu, Y. Z. Tan, X. Yuan, J. W. Chew, *J. Hazard. Mater.* **2018**, *347*, 412.

[141] J. Li, Y. Zhao, M. Xia, H. An, H. Bai, J. Wei, B. Yang, G. Yang, *Appl. Catal., B* **2019**, *261*, 118244.

[142] L. Di, H. Yang, T. Xian, X. Liu, X. Chen, *Nanomaterials* **2019**, *9*, 399.

[143] S. Zhu, X. Li, J. Kang, X. Duan, S. Wang, *Environ. Sci. Technol.* **2018**, *53*, 307.

[144] Y. Wang, S. Indrawirawan, X. Duan, H. Sun, H. M. Ang, M. O. Tadé, S. Wang, *Chem. Eng. J.* **2015**, *266*, 12.

[145] K.-Y. A. Lin, Y.-C. Chen, Y.-F. Lin, *Chem. Eng. Sci.* **2017**, *160*, 96.

[146] X. Pang, Y. Guo, Y. Zhang, B. Xu, F. Qi, *Chem. Eng. J.* **2016**, *304*, 897.

[147] P. Zeng, R. Ran, Z. Chen, W. Zhou, H. Gu, Z. Shao, S. Liu, *J. Alloys Compd.* **2008**, *455*, 465.

[148] S. B. Hammouda, F. Zhao, Z. Safaei, D. L. Ramasamy, B. Doshi, M. Sillanpää, *Appl. Catal., B* **2018**, *233*, 99.

[149] S. B. Hammouda, F. Zhao, Z. Safaei, V. Srivastava, D. Lakshmi Ramasamy, S. Iftekhar, S. kalliola, M. Sillanpää, *Appl. Catal., B* **2017**, *215*, 60.

[150] J. Miao, X. Duan, J. Li, J. Dai, B. Liu, S. Wang, W. Zhou, Z. Shao, *Chem. Eng. J.* **2019**, *355*, 721.

[151] X. Duan, C. Su, J. Miao, Y. Zhong, Z. Shao, S. Wang, H. Sun, *Appl. Catal., B* **2018**, *220*, 626.

[152] Y. Rao, Y. Zhang, F. Han, H. Guo, Y. Huang, R. Li, F. Qi, J. Ma, *Chem. Eng. J.* **2018**, *352*, 601.

[153] X. Tian, P. Gao, Y. Nie, C. Yang, Z. Zhou, Y. Li, Y. Wang, *Chem. Commun.* **2017**, *53*, 6589.

[154] M. Zhu, J. Miao, X. Duan, D. Guan, Y. Zhong, S. Wang, W. Zhou, Z. Shao, *ACS Sustainable Chem. Eng.* **2018**, *6*, 15737.

[155] P. Gao, X. Tian, Y. Nie, C. Yang, Z. Zhou, Y. Wang, *Chem. Eng. J.* **2019**, *359*, 828.

[156] Y. Chu, Y. Tan, Z. Shen, P. Liu, N. Han, J. Kang, X. Duan, S. Wang, L. Liu, S. Liu, *J. Hazard. Mater.* **2018**, *356*, 53.

[157] K.-Y. A. Lin, Y.-C. Chen, T.-Y. Lin, H. Yang, *J. Colloid Interface Sci.* **2017**, *497*, 325.

[158] Y. Rao, F. Han, Q. Chen, D. Wang, D. Xue, H. Wang, S. Pu, *Chemosphere* **2019**, *218*, 299.

[159] K.-Y. A. Lin, T.-Y. Lin, Y.-C. Lu, J.-T. Lin, Y.-F. Lin, *Chem. Eng. Sci.* **2017**, *168*, 372.

[160] T. Ma, L. Liu, B. Meng, J. Gao, S. Wang, S. Liu, *Sep. Purif. Technol.* **2019**, *211*, 298.

[161] M. Carbajo, F. J. Rivas, F. J. Beltrán, P. Alvarez, F. Medina, *Ozone: Sci. Eng.* **2006**, *28*, 229.

[162] F. J. Rivas, M. Carbajo, F. J. Beltrán, B. Acedo, O. Gimeno, *Appl. Catal., B* **2006**, *62*, 93.

[163] M. Carbajo, F. J. Beltrán, O. Gimeno, B. Acedo, F. J. Rivas, *Appl. Catal., B* **2007**, *74*, 203.

[164] M. Carbajo, F. J. Beltrán, F. Medina, O. Gimeno, F. J. Rivas, *Appl. Catal., B* **2006**, *67*, 177.

[165] F. J. Beltrán, P. Pocostales, P. M. Álvarez, F. López-Piñeiro, *Appl. Catal., B* **2009**, *92*, 262.

[166] F. J. Beltrán, P. Pocostales, P. Alvarez, J. F. García-Araya, O. Gimeno, *Ozone: Sci. Eng.* **2010**, *32*, 230.

[167] C. A. Orge, J. J. M. Órfão, M. F. R. Pereira, B. P. Barbero, L. E. Cadús, *Appl. Catal., B* **2013**, *140–141*, 426.

[168] K. M. Bulanin, J. C. Lavalley, A. A. Tsyganenko, *J. Phys. Chem. B* **1995**, *99*, 5.

[169] S. Afzal, X. Quan, J. Zhang, *Appl. Catal., B* **2017**, *206*, 692.

[170] Y. Zhang, Y. Xia, Q. Li, F. Qi, B. Xu, Z. Chen, *Sep. Purif. Technol.* **2018**, *197*, 261.

[171] Y. Zhang, Q. Li, Y. Long, J. Zou, Z. Song, C. Liu, L. Liu, F. Qi, B. Xu, Z. Chen, *Appl. Catal., B* **2019**, *254*, 569.

[172] J.-M. Wu, W. Wen, *Environ. Sci. Technol.* **2010**, *44*, 9123.

[173] E. Forgacs, T. Cserháti, G. Oros, *Environ. Int.* **2004**, *30*, 953.

[174] S. B. Hammouda, C. Salazar, F. Zhao, D. L. Ramasamy, E. Laklova, S. Iftekhar, I. Babu, M. Sillanpää, *Appl. Catal., B* **2019**, *240*, 201.

[175] S. Rahim Pouran, A. A. Abdul Raman, W. M. A. Wan Daud, *J. Cleaner Prod.* **2014**, *64*, 24.

[176] M. Sun, Y. Jiang, F. Li, M. Xia, B. Xue, D. Liu, *Mater. Trans.* **2010**, *51*, 2208.

[177] W. Zhong, T. Jiang, Y. Dang, J. He, S.-Y. Chen, C.-H. Kuo, D. Kriz, Y. Meng, A. G. Meguerdichian, S. L. Suib, *Appl. Catal., A* **2018**, *549*, 302.

[178] M. Y. Leiw, G. H. Guai, X. Wang, M. S. Tse, C. M. Ng, O. K. Tan, *J. Hazard. Mater.* **2013**, *260*, 1.

[179] G. A. Kimmel, N. G. Petrik, *Phys. Rev. Lett.* **2008**, *100*, 196102.

[180] A. Staykov, H. Téllez, T. Akbay, J. Druce, T. Ishihara, J. Kilner, *Chem. Mater.* **2015**, *27*, 8273.

[181] M. Sun, Y. Jiang, F. Li, M. Xia, B. Xue, D. Liu, *Mater. Trans.* **2010**, *51*, 1981.

[182] H. Chen, J. Motuzas, W. Martens, J. C. Diniz da Costa, *Appl. Surf. Sci.* **2018**, *450*, 292.

[183] F. Deganello, L. F. Liotta, A. Longo, M. P. Casaletto, M. Scopelliti, *J. Solid State Chem.* **2006**, *179*, 3406.

[184] F. Deganello, L. F. Liotta, S. G. Leonardi, G. Neri, *Electrochim. Acta* **2016**, *190*, 939.

[185] N. E. Trofimenko, H. Ullmann, *J. Eur. Ceram. Soc.* **2000**, *20*, 1241.

[186] O. P. Taran, A. B. Ayusheev, O. L. Ogorodnikova, I. P. Prosvirin, L. A. Isupova, V. N. Parmon, *Appl. Catal., B* **2016**, *180*, 86.

[187] X. Xu, C. Su, W. Zhou, Y. Zhu, Y. Chen, Z. Shao, *Adv. Sci.* **2015**, *3*, 1500187.

[188] H. Chen, J. Motuzas, W. Martens, J. C. Diniz da Costa, *J. Environ. Chem. Eng.* **2018**, *6*, 5870.

[189] E. Dvininov, U. A. Joshi, J. R. Darwent, J. B. Claridge, Z. Xu, M. J. Rosseinsky, *Chem. Commun.* **2011**, *47*, 881.

[190] G. Li, Y. Zhang, L. Wu, F. Wu, R. Wang, D. Zhang, J. Zhu, H. Li, *RSC Adv.* **2012**, *2*, 4822.

[191] Y. Xu, X. Li, X. Cheng, D. Sun, X. Wang, *Environ. Sci. Technol.* **2012**, *46*, 2856.

[192] V. Subbaramaiah, V. C. Srivastava, I. D. Mall, *AIChE J.* **2013**, *59*, 2577.

[193] N. Crowther, F. Larachi, *Appl. Catal., B* **2003**, *46*, 293.

[194] Y. Liu, D. Sun, *Appl. Catal., B* **2007**, *72*, 205.

[195] H. Ma, Q. Zhuo, B. Wang, *Environ. Sci. Technol.* **2007**, *41*, 7491.

[196] Y. Zhang, D. Li, Y. Chen, X. Wang, S. Wang, *Appl. Catal., B* **2009**, *86*, 182.

[197] A. E. de los Monteros, G. Lafaye, A. Cervantes, G. Del Angel, J. Barbier Jr., G. Torres, *Catal. Today* **2015**, *258*, 564.

[198] M. Yang, A. Xu, H. Du, C. Sun, C. Li, *J. Hazard. Mater.* **2007**, *139*, 86.

[199] H. Deng, L. Lin, Y. Sun, C. Pang, J. Zhuang, P. Ouyang, Z. Li, S. Liu, *Catal. Lett.* **2008**, *126*, 106.

[200] J. Faye, E. Guélou, J. Barrault, J. M. Tatibouët, S. Valange, *Top. Catal.* **2009**, *52*, 1211.

[201] P. Gao, N. Li, A. Wang, X. Wang, T. Zhang, *Mater. Lett.* **2013**, *92*, 173.

[202] M. Bernardi, F. A. Deorsola, D. Fino, N. Russo, *Waste Biomass Valorization* **2014**, *5*, 857.

[203] B. Palas, G. Ersöz, S. Atalay, *Chemosphere* **2018**, *209*, 823.

[204] S. Royer, B. Levasseur, H. Alamdari, J. Barbier, D. Duprez, S. Kaliaguine, *Appl. Catal., B* **2008**, *80*, 51.

[205] W. Sun, H. Wei, L. yang An, C. Jin, H. Wu, Z.-a. Xiong, C. Pu, C. Sun, *Appl. Catal., B* **2019**, *245*, 20.

[206] S. B. Hammouda, F. Zhao, Z. Safaei, I. Babu, D. L. Ramasamy, M. Sillanpää, *Appl. Catal., B* **2017**, *218*, 119.

[207] S. Sengodan, S. Ahn, J. Shin, G. Kim, *Solid State Ion* **2012**, *228*, 25.

[208] V. Gupta, M. Rakesh, *J. Water Process. Eng.* **2019**, *27*, 58.

[209] L. Zou, Q. Wang, Z. Wang, L. Jin, R. Liu, X. Shen, *Ind. Eng. Chem. Res.* **2014**, *53*, 658.

[210] C. Nie, Z. Dai, H. Meng, X. Duan, Y. Qin, Y. Zhou, Z. Ao, S. Wang, T. An, *Water Res.* **2019**, *166*, 115043.

[211] Z. Liu, B. Ren, H. Ding, H. He, H. Deng, C. Zhao, P. Wang, D. D. Dionysiou, *Water Res.* **2020**, *171*, 115456.

[212] S. Luo, B. Fu, F. Liu, K. He, H. Yang, J. Ma, H. Wang, X. Zhang, P. Liang, X. Huang, *Water Res.* **2020**, *172*, 115493.

[213] N. Sergienko, J. Radjenovic, *Appl. Catal., B* **2020**, *267*, 118608.

[214] H. Song, L. Yan, Y. Wang, J. Jiang, J. Ma, C. Li, G. Wang, J. Gu, P. Liu, *Chem. Eng. J.* **2019**, *391*, 123560.

[215] Q. Wang, S. Zhou, S. Xiao, F. Wei, X. Zhao, J. Qu, H. Wang, *RSC Adv.* **2018**, *8*, 14775.

**ADVANCED
SCIENCE NEWS**

www.advancedsciencenews.com

**ADVANCED
FUNCTIONAL
MATERIALS**

www.afm-journal.de

Kai Wang obtained his bachelor's degree from China University of Petroleum (East China) in 2016. Now, he is pursuing a Ph.D. degree in Chemical Engineering at Curtin University, Australia. His research interests are developing perovskite oxides-based materials and their application in advanced oxidation process.

Zongping Shao is a distinguished professor of chemical engineering at Curtin University, Australia, and Nanjing Tech University, China. He obtained his Ph.D. from Dalian Institute of Chemical Physics, China, in 2000. He worked as a visiting scholar at Institut de Researches Sur La Catalyse, CNRS, France, and postdoc at California Institute of Technology, USA, from 2000 until 2005. His current research interests include solid oxide fuel cells, lithium-ion batteries, oxygen-permeable membranes, and low-temperature energy conversion devices. He has been recognized as a highly cited researcher by Clarivate Analytics since 2017.

Shaomin Liu is a professor in the Department of Chemical Engineering at Curtin University. He received his Ph.D. degree from the National University of Singapore in 2002, and then worked as a postdoctoral research fellow in Chemical Engineering at the California Institute of Technology from 2002 to 2005. From the end of 2008, he has been working at Curtin University, Australia. His research interests include inorganic membranes for gas separation, membrane reactors for gas reactions, nanoporous materials, solid oxide fuel cells, bioceramics, nanoparticles for antimicrobial property, and advanced oxidations for water treatment.